Behavior of Citrate-Capped Ultrasmall Gold Nanoparticles on a Supported Lipid Bilayer Interface at Atomic Resolution

Rashad Kariuki, Rowan Penman, Saffron J. Bryant, Rebecca Orrell-Trigg, Nastaran Meftahi, Russell J. Crawford, Chris F. McConville, Gary Bryant, Kislon Voïtchovsky, Charlotte E. Conn, Andrew J. Christofferson,* and Aaron Elbourne*

Abstract:

Nanomaterials have the potential to transform biological and biomedical research, with applications ranging from drug delivery and diagnostics to targeted interference of specific biological processes. Most existing research is aimed at developing nanomaterials for specific tasks such as enhanced biocellular internalization. However, fundamental aspects of the interactions between nanomaterials and biological systems, in particular, membranes, remain poorly understood. In this study, we provide detailed insights into the molecular mechanisms governing the interaction and evolution of one of the most common synthetic nanomaterials in contact with model phospholipid membranes. Using a combination of atomic force microscopy (AFM) and molecular dynamics (MD)simulations, we elucidate the precise mechanisms by which citrate-capped 5 nm gold nanoparticles (AuNPs) interact with supported lipid bilayers (SLBs) of pure fluid (DOPC) and pure gel-phase (DPPC) phospholipids. On fluid-phase DOPC membranes, the AuNPs adsorb and are progressively internalized as the citrate capping of the NPs is displaced by the surrounding lipids. AuNPs also interact with gel-phase DPPC membranes where they partially embed into the outer leaflet, locally disturbing the lipid organization. In both systems, the AuNPs cause holistic perturbations throughout the bilayers. AFM shows that the lateral diffusion of the particles is several orders of magnitude smaller than that of the lipid molecules, which creates some temporary scarring of the membrane surface. Our results reveal how functionalized AuNPs interact with differing biological membranes with mechanisms that could also have implications for cooperative membrane effects with other molecules.

Nanomaterials are widely reported as advanced biomedical technologies, often showing promise where other macroscale approaches have failed. For example, nanoparticles (NPs) have been investigated as drug delivery vehicles,[1] nanomedicines,[2] emerging antimicrobials,[3] disease diagnostics,[4] cellular-imaging tools,[5] and tumor (cancer) treatments,[6] among others.[2−4,7] The commonality between most nanoparticle-based technologies is the need to interact with, alter, and/or transverse a cell's outer membrane in order to fulfill their function.[1−3] This biological membrane serves as the protective barrier that isolates the internal cell environment from the surroundings and poses a challenge for nanomaterial internalization,[13] with considerable research focused on tailoring nanomaterials to facilitate this task.[4−6] Strategies include functionalization of metal nanoparticles,[7−9] the use of nano-objects with various shapes[10−12] and altering the NPs surface chemistry,[13−15] as well as employing biological[16−19] and polymeric[20,21] NPs. In all of these systems,[22−25] the approach often relies on mimicking the hydrophilicity profile of the membrane[26] or finding ways to interact with or avoid specific cellular components (proteins, lysosomes, organelles, etc.).[27−32] The underlying challenge is to achieve control of the membrane−nanomaterials interactions, a task complicated by the large number of different biomolecules present in most biomembranes.

Phospholipids make up the bulk of the biomembrane, forming a continuous bilayer that is the universal component of all cell membranes.[18,22,23,25] Other biomolecules such as proteins and sugars can be embedded or anchored in this bilayer structure, ensuring the functionality of the membrane for cellular-scale processes such as transmembrane trafficking, budding, endocy- tosis, and protein-mediated channel regulation.[18,22,23,25] The lipids not only play a passive role in hosting functional biomolecules but also play an active role in locally modulating the membrane mechanical properties in response to external stimuli and by being involved in adapting the molecular composition of both lipids and proteins to best support the needs of the cell.[26,27] It is therefore crucial to derive a comprehensive understanding of the nanomaterial−lipid interactions (i.e., adsorption,[12] desorption,[8] translocation,[28] and internalization/uptake[9,29]) at the molecular level to achieve the desired application goal. Several experimental studies have outlined interactions between gold NPs (AuNPs) and model membranes, including their adsorption dynamics.[33−36] In tandem, computational simulations have analyzed interfacial nanomaterial−supported lipid bilayer (SLB) interactions.[37−39] Results highlight the importance of the particle composition, ligand-cap dynamics, and the underlying membrane composi- tion. AuNP inclusions can disrupt the mechanical stability and normal ordering of the bilayer,[23,33−39] but the molecular interactions that underpin these processes are far from trivial. The lipid headgroup chemistry, the solution properties,[40] and the precise adsorption of nanomaterials can all influence the macroscopic properties of the membrane.[41]

To date, our understanding of the general features under-pinning the interactions of nanomaterials with biomembranes remains limited for several reasons. First, the majority of studies tend to focus on the properties specific to a given material, functionalization, or on its ability to achieve a particular task with respect to biological systems.[6,8,9,16,17] Second, academ- ic[1,4,10] and medical studies[42] have typically focused on the biological responses of living cells to nanomaterials via nonspecific bioassays, which provide limited information about the mechanics of the nanomaterial−molecular level interactions during the biophysical response.[43] This is partially because observations at the nanometer scale can be hard to track on living cells in real time.[2] When available,[22,44,45] results often lack the contextual information about the nanoscale environ- ment of a given nano-object to relate interaction with function. As a result, global properties are favored such as nanomaterial- induced changes in the cell membrane stiffness, physicochem- istry, and adhesive properties.[14−16] More quantitative studies are needed which follow single nano-objects in situ as they interact with biomembranes and with sufficient resolution to gather contextual information about the impact of the object on the organization and evolution of the membrane.

Here, we provide such fundamental insights by focusing on a system simple enough to allow for a clear interpretation of the results. To do this, we investigate the interaction of AuNPs with phospholipid bilayers in fluid and gel phases. Noble metal NPs are among the most common type of NPs and can be functionalized for various tasks, usually through the formationof a self-assembled monolayer on the particle's surface.[46] This coating is also necessary to ensure the stability of the particle given its small size. In this study, we use citrate-capped AuNPs,[47−49] the default capping and arguably the most common form also widely available commercially.[48−54] The model biomembranes are also kept as simple as possible, using in each case only one type of lipid molecule. This is to identify in detail the generic interactions and processes likely to play a role in most systems where NPs interact with biomembranes. We selected lipids with zwitterionic headgroups to avoid probing obvious electrostatic interactions. We comparatively examine fluid- and gel-phase bilayers since the mobility of the molecules in the membranes is a key physical parameter in controlling the evolution and fate of a given system. We use SLBs where the membrane is loosely adhered to a solid substrate, but maintaining a ∼1 nm thick water layer[55] which preserves molecular mobility within the bilayer.[56−58] Synthetic SLBs[18,19] are often used as model systems for studying the fundamental biophysical processes of cell membranes,[17,20] because they offer full control of the model membranes both chemically and structurally.[59−61] The fact that SLBs are supported is also arguably a better representation of the crowded cell-wall environment where biomembranes are heavily constrained by the supporting cytoskeleton as well as often the glycocalyx.[62,63] To carefully follow the evolution of our model system, we use a combination of atomic force microscopy (AFM) in solution and molecular dynamics (MD) simulations. The former provides local insight at the scale of single NPs while also allowing for contextual information over the scale of hundreds of nanometers around the NPs of interest. AFM can be used to track the evolution of the system over a time period from tens of seconds to hours, matching the relevant biological time scales. Complementarily, MD offers precise atomistic insights into the interactions and possible penetration of NPs in the bilayers, highlighting the relevant molecular motions and mechanisms. The time scales accessible in MD are consistently shorter but allow tracking of known phenomena such as ligand exchange mechanisms.[38,64,65]

Our systems comprise citrate-capped AuNPs, with a nominal diameter of 5 nm, at the interface of an artificial biomembrane. SLBs of pure 1,2-di(9Z-octadecenoyl)-*sn*-glycero-3-phospho- choline (DOPC) and 1,2-dipalmitoyl-*sn*-glycero-3-phospho- choline (DPPC) were self-assembled atop a muscovite (mica) surface (Figure 1) and represent liquid-phase (fluid) (L_α) and gel-phase (L_β) lipid bilayers, respectively. These systems provide insight into the differing behavior of ultrasmall, citrate-capped AuNPs at these biointerfaces. Figure 1 shows a stylized schematic of these systems using constituents from the MD simulations.

RESULTS AND DISCUSSION

Atomic Force Microscopy Investigation. High-resolu- tion amplitude-modulated (AM)-AFM imaging was conducted in liquid using small-amplitude imaging protocols previously developed for interfacial imaging of ionic solutes,[40,48−52] viscous fluids,[45,47,53−58] and soft matter interfaces.[33,59] For all experi- ments, surface-adsorbed flat lipid bilayers were formed via the previously reported vesicle fusion method (see Figure S1).[19,41,42] Figure 2A shows representative low-resolution (5 μm × 5 μm) and high-resolution (500 nm × 500 nm, insert) AFM height images of a DOPC SLB. The bilayer surface is relatively homogeneous, with spatially dispersed defects (see Figure 2A). Examining a smaller region of the surface (indicated

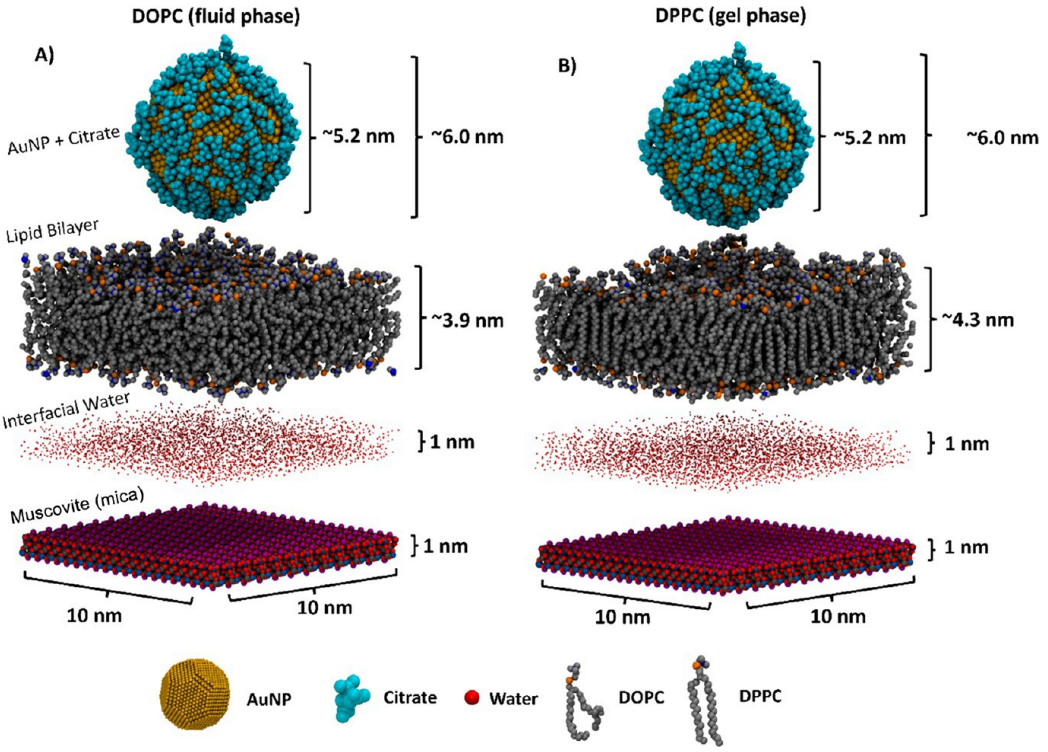

Figure 1. Schematic overview of the systems studied in this work by AFM and MD simulations. (A) DOPC and (B) DPPC are investigated as model supported lipid bilayers at the mica interface. The systems are first investigated as pure lipid bilayer systems (without AuNPs) to provide a baseline for comparison with systems where AuNPs are introduced. The AuNPs are nominally ~5 nm in size with a dynamic citrate ligand shell adsorbed to the surface of the AuNP for a total diameter of ~6 nm. Muscovite is used as a typical support structure for the formation of uniform SLBs, and a layer of interfacial water is known to form between the solid substrate and the bilayer with a surface-normal width of ~1 nm. The water layer above the membrane, and NaCl ions (150 mM) are not shown. A schematic key is shown at the bottom of the images. Hydrogen atoms are not shown, and lipid phosphate groups are represented as a single orange bead centered on the phosphorus atom for clarity.

by the blue box, Figure 2A) shows that the lipid bilayer surface is relatively unremarkable (see Figure 2A, inset). These images are commensurate with a flat, continuous adsorbed lipid bilayer. In a standard AFM experiment, such as that performed here, no direct chemical data is provided, meaning that confirming the presence of a continuous lipid bilayer cannot be achieved by images alone since the bilayer appears as smooth as the underlying mica surface. To confirm the presence of the lipid bilayer, we used force spectroscopy (Figure 2B); the AFM tip is moved toward the substrate at a selected location while tracking the force it experiences. These so-called *force curves* show a characteristic step as the tip ruptures the bilayer when pressing with more than ~3 nN force (Figure 2B). The rupture force depends on many parameters including the tip geometry, the type of lipids composing the bilayer, and the environment, but it unambiguously indicates the presence of a bilayer. Past the rupture point, the cantilever then presses on the mica substrate supporting the DOPC membrane, revealing a total bilayer thickness close to ~5 nm, consistent with previous AFM investigations.[19,60−63] This assertion is further supported by analysis of supported lipid bilayer patches (SLBPs) which are formed at lower concentrations (see Figure S2). Figure S1 and its supported text provides further explanation in the Supporting Information.

Following confirmed SLB formation, a 1 μL aliquot of the AuNP solution (5×10^{13} particles/mL) was introduced to the system, meaning that ~5×10^{10} particles could equilibrate with the SLB. The citrate-capped AuNPs employed in this study were confirmed to be face-centered cubic (fcc) with a diameter of 5.0 ± 0.6 nm by transmission electron microscopy and dynamic light scattering (see Figure S4). The underlying mica surface is circular with a diameter of 1 cm, equivalent to ~700 particles/μm^2. It should be noted, however, that this is only an estimate, and the number of surface-bound AuNPs is expected to be lower than this, as not all particles will migrate to the interface from solution immediately.

Figure 2C shows representative 5 μm × 5 μm AFM height images of a DOPC SLB following addition of the AuNPs. This image was collected a few minutes after AuNP exposure (see also Figure S5 for the associated phase data). Visual inspection of the image reveals distinct protrusions at various locations. Interestingly, the defects, or "holes", noted in the pure DOPC system have vanished from the SLB. The protrusions appear as three subtly different entities atop the SLB, which have been highlighted by different colored arrows: (1) individual, stable dots with a size less than 10 nm (blue arrows); (2) larger, aggregate-like structures (green arrows); and (3) streak-like marks (yellow arrows). As AuNPs are the only new material added to the system, the observed structures can be ascribed to the AuNPs and interpreted as follows: (1) the individual dots are attributed to surface-adsorbed, individual AuNPs from solution (Figure 2E); (2) the larger structures are aggregates of two or more AuNPs, which are expected in nanoparticle systems without strong stabilizing agents (such as those investigated here); and (3) the streak marks are a scan artifact caused by the dislodgement of AuNPs by the AFM tip. The latter is expected for loosely adsorbed material as it can be readily moved by the tip−sample forces applied during AFM imaging.[71] This could

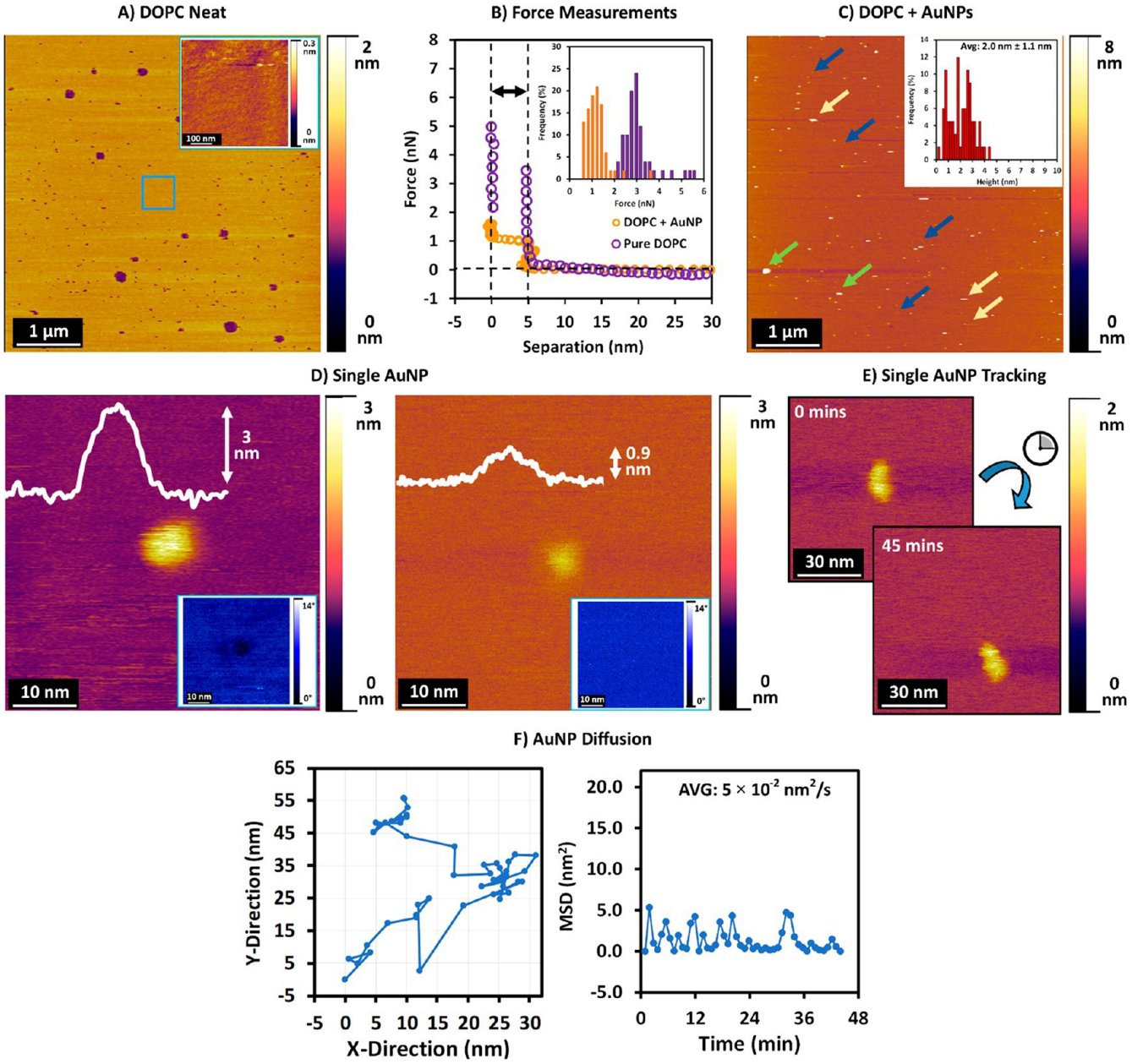

Figure 2. DOPC SLBs at the mica interface with and without AuNPs. High-resolution AFM images of (A) A SLB formed on a mica substrate via self-assembly (vesicle fusion method). (B) Force curve profile of the pure DOPC SLB (purple) and DOPC + AuNPs systems (orange). The inset shows a histogram of the average bilayer rupture force for both systems (n = 50 force curves). Raw deflection vs. distance data is provided in Figure S3. (C) A 5 μm × 5 μm height image of a DOPC SLB obtained following introduction of the AuNPs (concentration: 5.5 × 10^{13} particles/mL). The blue arrows point to adsorbed particles; the yellow arrows show streak lines in the image, where the AuNPs are moved by the AFM cantilever due to their adsorption not being complete, and the green arrows show AuNP aggregates. The inset shows the average particle height of 50 AuNPs adsorbed to the underlying SLB as a histogram. (D) 80 nm × 80 nm height images of a AuNP during SLB adsorption (left) and/or inclusion (right). Phase data are shown as insets (bottom right). The height difference is shown by the overlaid height profile representing the comparative height of the AuNP above the bilayer. Note: it appears less than the expected ~5 nm measured from TEM in both cases (see Figure S4). (E) Example time-lapse images obtained in the same scan region, highlighting that the particle is not static but rather slightly mobile. (F) (Left) Particle position monitored from the central point of the particle as a function of time from the series of images represented in panel E. (Right) Mean squared displacement (MSD) of the particle across/within the DOPC membrane plotted as a function of time.

highlight regions at which AuNP adsorption was incomplete or comparatively weaker than at other places.

Force spectroscopy of the DOPC SLB−AuNP system reveals on average a subtly different force profile compared to the DOPC (see Figure 2B). The apparent membrane thickness remains ~5 nm, but the required rupture force significantly decreases to 1.2 ± 0.5 nN (Figure 2B, inset). This represents a 60% reduction compared to the pure DOPC system. The fact that the force decreases rules out possible tip aging or blunting which would have the opposite effect. Further, the force profiles routinely appeared less distinct, with wobbles and less distinct "jump-ins", despite identical acquisition settings. This hints at the presence, or uptake/incorporation, of the AuNPs causing destabilization of the SLB.

The evolution of single, surface-adsorbed AuNPs is exemplified by Figure 2D (right) where the initial height of ~3 nm progressively reduces to ~0.9 nm. Moreover, the particle subsequently is no longer visible in the phase data (see Figure 2D, insets). While the precise interpretation of the phase contrast is not simple, it is sensitive to the stiffness of the sample.[123] Here, this indicates that the stiffer AuNP is initially exposed to the cantilever and responsible for the contrast in phase data but gets progressively embedded into the membrane (Figure 2D) as the contrast decreases due to the gentle imaging conditions. This interpretation is confirmed by a survey of particle heights taken from multiple AFM images, which showed an average value of 2 ± 1.1 nm (see Figure 2C, inset). Considering the average measured thickness of the bilayer (~5.5 nm), and that of the estimated solvation layer between the bilayer and mica surface (~1 nm), we assume that the ~5 nm AuNPs are not touching the mica surface but are embedded within the bilayer core, thus enabling their diffusion across/within the bilayer without directly interacting with the mica.

To track the dynamics of the AuNPs once embedded in the membrane, time-lapse AFM images of a single AuNP show its diffusion into the membrane (Figure 2E). The time interval between two consecutive images is ~40 s. The particle's position appears to move over time, and its center of mass was tracked for ~45 min (Figure 2F, left). From the mean squared displacement of the particle over time, we estimate its 2D diffusion to be D_{NP} ~ 0.5 nm^2/s (Figure 2F, right). To assess whether this value is significantly influenced by the scanning AFM tip, the AFM imaging force was estimated during these experiments. We found a maximum value of 0.2 nN (see Figure S6), comparable to the force stabilizing individual proteins or lipids in a bilayer.[66−68] Considering the relatively large number of lipid molecules in contact with the NPs, the force exerted by the tip should not be sufficient to appreciably affect the NPs' diffusion. In addition, this small imaging force was coupled with brief, intermittent tip−sample contact, because in AM mode the cantilever is oscillated, so it does not drag across the sample. Finally, the nanoparticle does not just move back and forth but rather in random directions.

The gel-phase DPPC lipid system was then investigated using the same protocols as outlined for the DOPC system (see Methods). Figure 3A shows a representative low-magnification (left) and higher-resolution (right) AFM image of a DPPC SLB. Phase data for the low-magnification image is shown in Figure S7. Defects are occasionally visible indicating a ~5.8 nm bilayer thickness, consistent with previous AFM studies.[69−71] As with DOPC, the DPPC bilayer formation was further confirmed by force spectroscopy, which revealed a higher elastic region of the DPPC membrane (as opposed to the DOPC), however, with a similar average rupture force of 3.0 ± 0.9 nN (Figures 2B and 3B). The similar rupture force of DOPC and DPPC may seem counterintuitive (i.e., it may be expected to be higher in a gel-phase system such as DPPC), but it is likely due to inherent experimental differences between the tips used for each measurement. Importantly, the qualitative differences between curves are self-consistent and still highlight differences between the DOPC and DPPC systems. The step width of 6 nm is slightly larger than that for DOPC, which is consistent with the presence of a DPPC bilayer. Together, these data confirm the presence of a single DPPC bilayer at the mica interface, as well as DPPC SLBP assessment (see Figure S2).

After successful SLB formation, the same aliquot of 5 nm AuNPs (5.5×10^{13} particles/mL) was introduced into the system. Protrusions over the bilayer are visible after adjunction of the AuNP (Figure 3C), with an average height distribution of 4.3 ± 1.9 nm (Figure 3C). Due to the known particle size (as characterized via TEM and DLS in Figure S4), we can assume these particles to be primarily atop the bilayer, with minimal embedding. This is further corroborated by the phase data (see Figure 3D, insets), which shows nonuniform phase maps on the imaged surfaces. The required rupture force was seen to decrease to ~1.6 ± 1.4 nN, compared to the pure DPPC system (cf. Figures 3B, inset). The decrease in rupture force indicates a potentially destabilizing effect of the AuNPs on the membrane structure; notably the observed rupture events are not seen cleanly in the separation data in Figure 3B. This is another strong indication of the destabilizing effects.

The dynamics of single AuNPs were also investigated using time-lapse AFM. The inset in Figure 3D shows the height profile of a single AuNP after adsorption onto the DPPC SLB. The AuNP protrudes roughly 3 nm out of the membrane, indicating partial embedding. Position tracking (see Figure 3F) yields a 2D diffusion rate of ~3.6×10^{-3} nm^2/s; 1 order of magnitude lower than that for the fluid-phase DOPC. The observed AuNP inclusions in the DPPC SLB were at a shallower depth within the bilayer compared to the DOPC SLB. However, even with the reduced penetration depth, the AuNPs were still able to impart interfacial mechanical changes in the bilayer as characterized via the reduced rupture force (Figure 3B). The AuNP also exhibited greatly reduced diffusion within the DPPC SLB as compared to the DOPC SLB (see Figures 2 and 3).

Molecular Dynamics Simulations. MD simulations were employed to gain atomistic insight into the behavior of citrate-capped AuNPs and their interactions with the DOPC and DPPC bilayer systems investigated experimentally (see Figure 4 and Figure 5). Simulation components were selected to adequately recreate the experimental in situ AuNP SLB systems discussed above. As such, the simulated systems included a single basal plane 10 nm (X) × 10 nm (Y) mica substrate, a lipid bilayer (either DOPC or DPPC), an intervening ~1 nm thick adlayer of water,[72−74] which resides between the substrate and the lipid bilayer, and a solvated citrate-capped AuNP. The system itself can then be thought of as two components: (1) the supported bilayer, which includes the substrate, the water solvation layer, and the lipid bilayer, and (2) the solvated citrate-capped AuNP. The pure supported lipid bilayers were first separately equilibrated for DOPC and DPPC, which provided a baseline for analysis (see Figures S8 and S9, respectively). In general, these data revealed stable bilayer systems with the characteristic structure and behavior expected for a fluid-phase (DOPC) and gel-phase (DPPC) system. The complete bilayer system for analysis of adsorption consisted of the SLB and the citrate-capped AuNP. Adjustments to the pairwise nonbonded interactions between gold and the other atoms were made to reproduce the experimental citrate coverage and exchange (further discussion in Supporting Information) and were deemed successful once the citrate surface coverage reached ~157 citrate ions, in line with literature values.[50,75,76]

MD simulations of the citrate-capped AuNP−DOPC SLB systems were performed for 300 ns of simulation time. The citrate-capped AuNP was free to move within the simulation environment, and the citrate was not locked to the particle, meaning that it could displace as a function of interactions with the chemical environment. Figure 4A shows incremental snapshots of the system every 100 ns of simulation run time. Visual inspection of these snapshots qualitatively shows (1) the

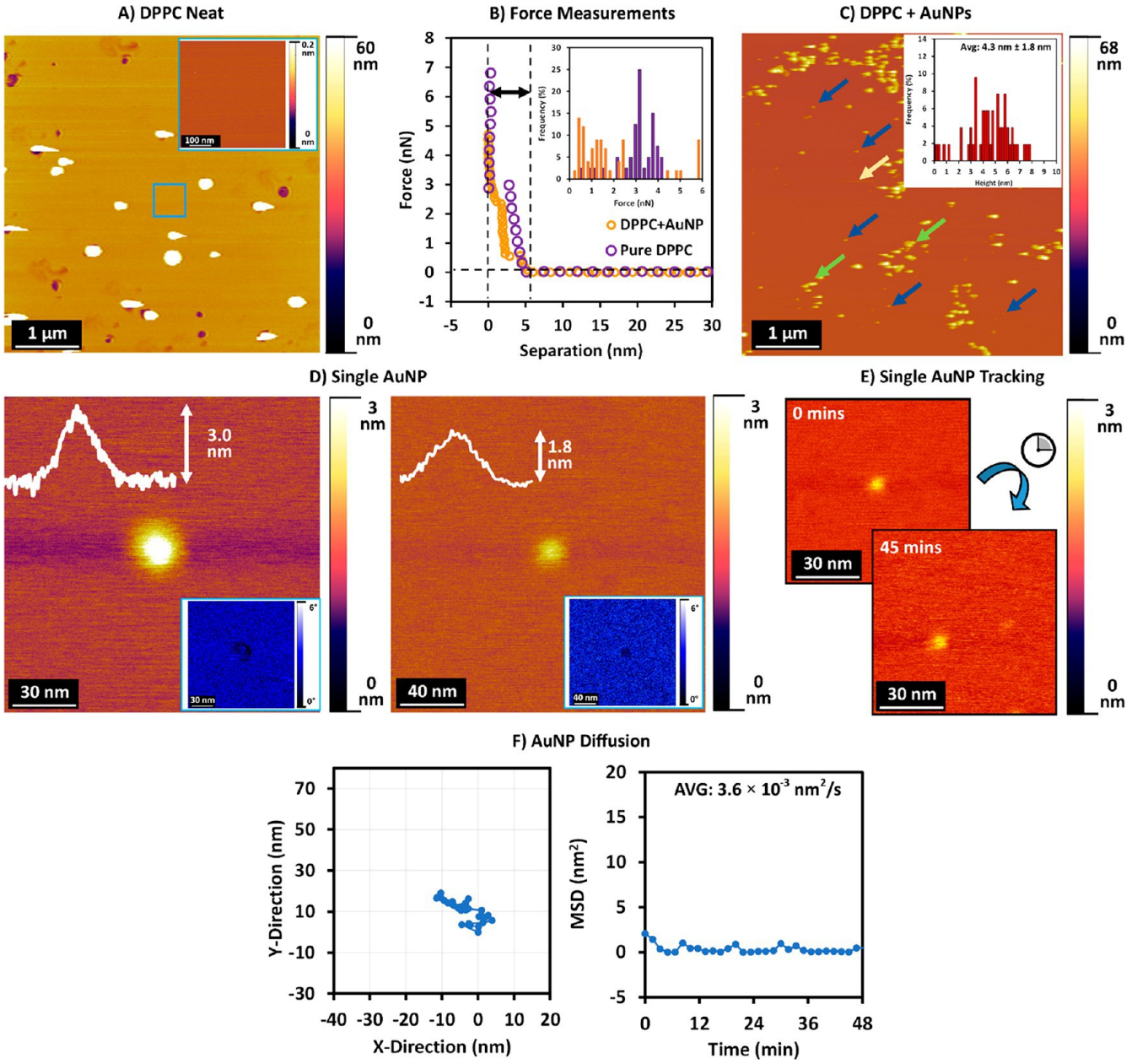

Figure 3. DPPC SLBs at the mica interface with and without AuNPs. High-resolution AFM images of (A) A SLB formed on a mica substrate via self-assembly (vesicle fusion method). (B) Force curve profile of the pure DPPC SLB (purple) and DPPC + AuNPs systems (orange). The inset shows a histogram of the average bilayer rupture force for both systems (n = 50 force curves). (C) A 5 μm × 5 μm height image of a DPPC SLB obtained following introduction of the AuNPs (concentration: 5.5 × 10^{13} particles/mL). The blue arrows point to adsorbed particles; the yellow arrows show streak lines in the image, where the AuNPs are moved by the AFM cantilever due to their adsorption not being complete, and the green arrows show AuNP aggregates. The inset shows the average particle height of 50 AuNP adsorbed to the underlying SLB as a histogram. (D) 80 nm × 80 nm height images of a AuNP during SLB adsorption (left) and/or inclusion (right). Phase data are shown as insets (bottom right). The height difference is shown by the overlaid height profile representing the comparative height of the AuNP above the bilayer. Note: it appears less than the expected ~5 nm measured from TEM in both cases (see Figure S4). (E) Example time-lapse images obtained in the same scan region, highlighting that the particle is not static but rather slightly mobile. (F) (left) Particle position monitored from the central point of the particle as a function of time from the series of images represented in Figure 3E. (right) Mean squared displacement (MSD) of the particle across/within the DPPC membrane plotted as a function of time.

initial system (0 ns), (2) initial particle adsorption and citrate displacement (100 ns), (3) further citrate displacement and particle uptake within the SLB (200 ns), and (4) particle engulfment (300 ns). Simultaneously, increased order can be observed in the SLB lipids as a function of time and particle inclusion within the SLB (see Figure 4A). The MD simulations were then quantitatively analyzed to better understand the behavior and dynamics of the observed particle adsorption and subsequent SLB internalization.

Figure 4B shows the vertical position of the citrate-capped AuNP relative to the DOPC SLB calculated from the center of mass (CoM) (solid yellow line) and outer radius (dashed line, top and bottom) of the particle as a function of time. All values here are measured as the average position of the AuNP CoM

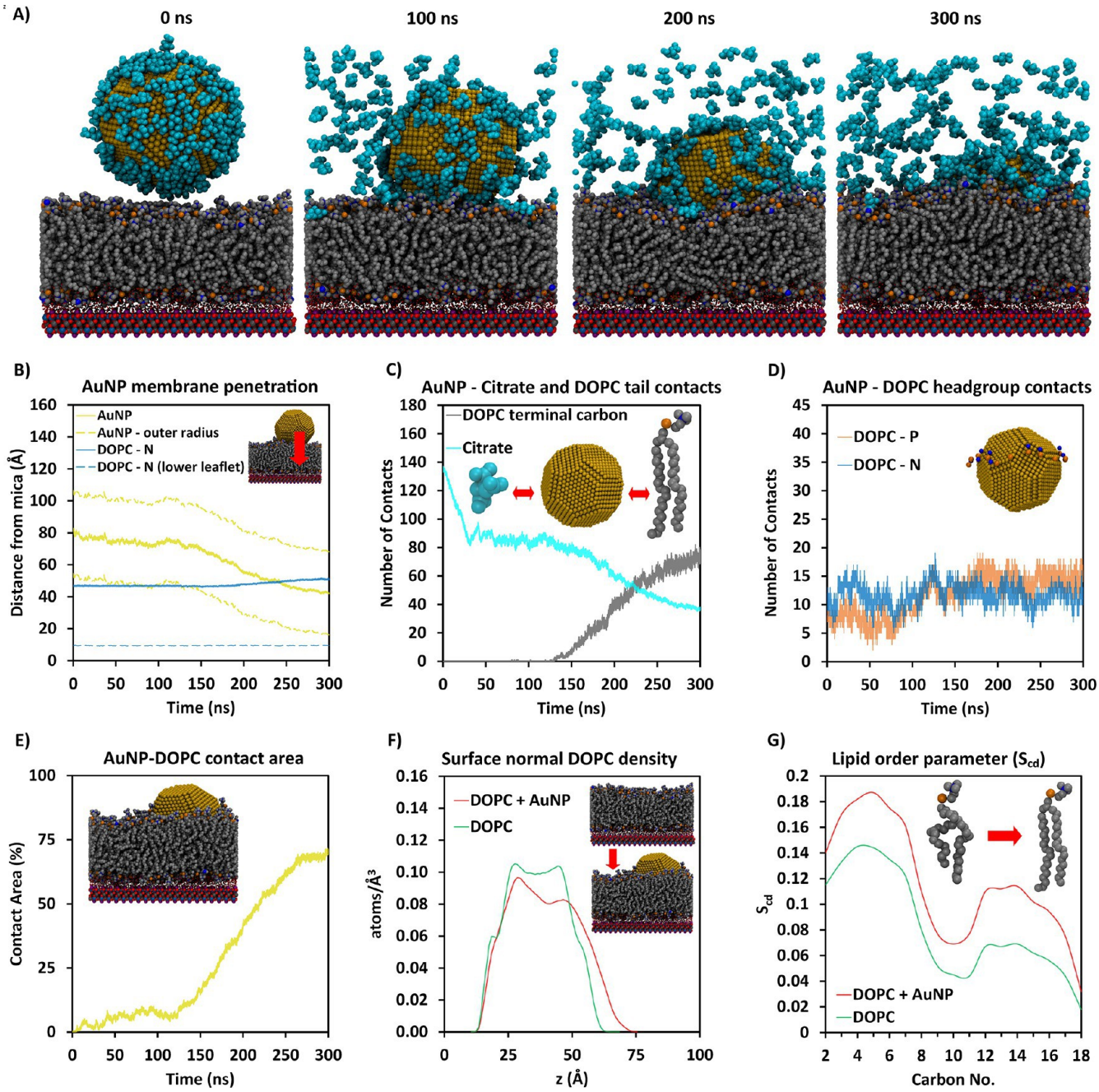

Figure 4. (A) MD simulation snapshots of the mica−DOPC−AuNP system. Movie S1 shows this process in more detail. (B) AuNP membrane penetration, as measured by the center-of-mass z position of the AuNP compared to DOPC trimethylamine nitrogen atom position as a function of time. (C) AuNP−citrate/terminal (tail) carbon contacts as a function of time. (D) AuNP−DOPC headgroup contacts as a function of time. (E) Membrane contact area between the AuNP and the DOPC interface. (F) Lipid atomic density in the z direction. (G) Lipid order parameter (S_{cd}).

along the z-axis relative to the mica surface terminal oxygens. The data shows that the AuNP was able to penetrate past the outer headgroups of the lipid bilayer and into the hydrophobic tail region of the lower leaflet. However, the particle was not capable of penetrating the phosphate or trimethylamine headgroups of the lower lipid leaflet and remained in the central hydrophobic core of the bilayer. The particle is observed to reach equilibrium at ~250 ns of simulation time. The AuNP was also observed to have minor lateral diffusion through the membrane (see Figure 4A and Movie S1). This is likely due to the linear lateral diffusion rate of the DOPC and the subsequent ability for the particle to diffuse within the system. This is not unexpected as DOPC is in the fluid phase at 303.15 K, meaning that a certain degree of intermolecular movement between lipid molecules is expected within an SLB. Indeed, the lateral diffusion coefficient value of DOPC lipids is reported to be ~1−10 $\mu m^2\ s^{-1}$, which likely allows AuNP diffusion through the SLB system.[77−79] Interestingly, similar diffusive behavior was observed in the time-lapse AFM data discussed above (see Figure 2E). Together, the simulated citrate-capped AuNP−DOPC SLB system is in good agreement with observations made from the AFM data discussed above (see Figure 2).

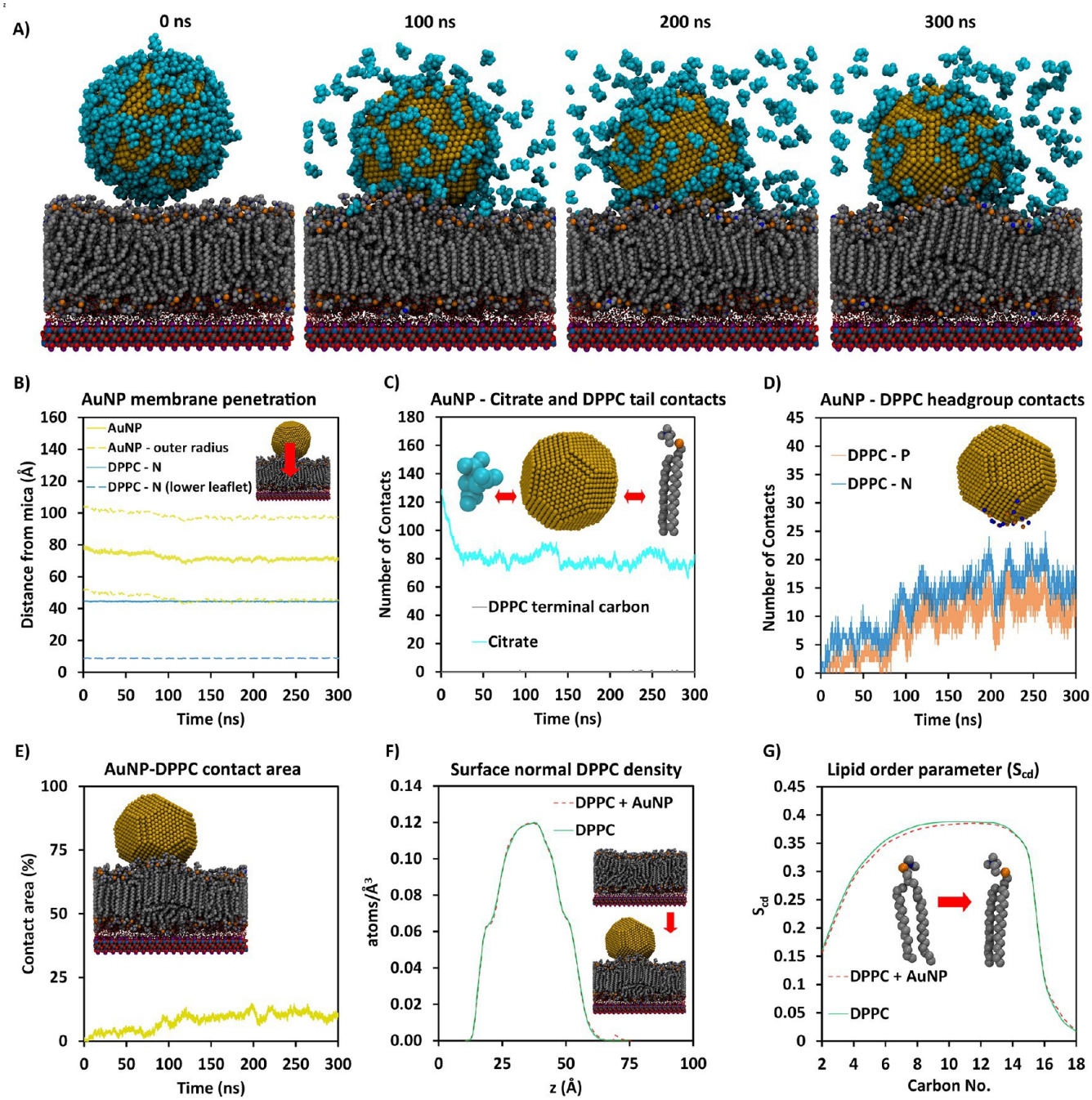

Figure 5. (A) MD simulation snapshots of the mica−DPPC−AuNP system. Movie S2 shows this process in more detail. (B) AuNP membrane penetration, as measured by the center-of-mass z position of the AuNP compared to DPPC trimethylamine nitrogen atom position as a function of time. (C) AuNP−citrate/terminal (tail) carbon contacts as a function of time. (D) AuNP−DPPC headgroup contacts as a function of time. (E) Membrane contact area between the AuNP and the DPPC interface. (F) Lipid atomic density in the z direction. (G) Lipid order parameter (S_{cd}).

Figure 4C shows the relative contact of the citrate (aqua line) and terminal carbon (gray line) to the surface of the AuNP as a function of time. This was counted based on a radial threshold of within 0.6 nm of the AuNP surface. Importantly, it was observed that the citrate cap of the AuNP dissociated from the gold surface during the adsorption process, and the relationship between the citrate contacts and lipid contacts was inversely proportional (i.e., the greater the lipid contacts, the fewer the citrate contacts). It was observed that the citrate molecules were exchanged for lipid headgroup and tail interactions during the production run, corresponding to increased DOPC contacts and a reduction in citrate contacts of ~80 (Figure 4A,C). It must be noted that, experimentally, the AuNP is capable of polarization, which means that the citrate should interact with the AuNP through the carboxylate surface charge interactions.[51] Due to limitations of classical MD simulations, the citrate is attracted through the van der Waals carbon and oxygen interactions. However, the parameter modulation allowed for similar approximate behavior to what is observed experimentally (i.e., average surface coverage and citrate displacement). The relative

interaction of the zwitterionic headgroups of the DOPC lipids to the AuNP was also considered as a function of time (see Figure 4D). These data were calculated as the number of headgroup phosphorus and trimethylammonium nitrogen atoms within 0.6 nm of the AuNP surface, revealing a constant number of trimethylamine contacts and increasing phosphorus contacts as the AuNP penetrated deeper into the membrane (i.e., from ~150 ns onward). Figure 4E shows the contact area as derived from the solvent-accessible surface area of both the membrane and the AuNP. Over the course of the simulation, the AuNP−DOPC contact area increased to a maximum of ~72%.

Figure 4F shows the lipid density for the final 10 ns of the simulation trajectory for the pure DOPC SLB and AuNP−DOPC SLB systems. In contrast to the pure DOPC SLB system (see Figure S8), the AuNP−DOPC SLB shows a distinct reduction in central lipid density, coupled to an increase in density at larger z values, as the AuNP displaces the DOPC (see Figure 4F). Local lipid molecules can be observed to slightly "creep" up the surface of the AuNP (see Figure 4A and Movie S1). The effect of the AuNP on the SLB is further described by calculation of lipid tail deuterium order parameter (S_{cd}) in the pure DOPC SLB system and the AuNP−DOPC SLB system (Figure 4G). The S_{cd} provides a measure of the lipid orientation, with a value of ±0.5 corresponding to C−H bond alignment perpendicular to the bilayer surface and deviations from ±0.5 associated with increasing disorder. Figure 4G shows the S_{cd} of the bilayer during particle interaction versus the equilibrated membrane state. The S_{cd} indicates a stiffening of the lipid chain, characterized by a shift toward 0.5 for the entire chain during AuNP interaction. This increased order exhibited by the lipid chains can be attributed to the compression caused by the reduction in available volume as the AuNP penetrates the membrane. This localized ordering of the lipid chains due to the presence of the AuNP could potentially contribute to the destabilization of the bilayer at larger length scales. This is discussed further below.

MD simulations of the pure DPPC SLB and AuNP−DPPC SLB were also performed (see Figure 5) under the same conditions to compare the behavior of the fluid-phase system to that of a gel-phase system, and to provide further insight into the DPPC AFM data discussed above (see Figure 3). MD data from the pure DOPC and DPPC systems can be found in Figures S8−S16. Figure 5A shows MD simulation snapshots of the citrate-capped AuNP−DPPC SLB systems at 100 ns simulation intervals. Visual inspection of these snapshots shows the qualitative differences of the DPPC system when compared to the DOPC systems (cf. Figure 4A and Figure 5A), including (1) the initial system (0 ns), (2) initial particle adsorption and minor citrate displacement (100 ns), (3) the particle arresting in the z-plane and not penetrating further into the bilayer, and (4) the particle reaching z-plane equilibrium with partial citrate displacement and only partial bilayer inclusion (300 ns). The diminished inclusion of the particle within the bilayer is commensurate with the AFM data (see Figure 3), where relative bilayer adsorbed particle heights were larger for this system than for DOPC. These data suggest distinct differences between the behavior of the AuNP at the fluid-phase and gel-phase lipid interface. Interestingly, local bilayer distortion is observed below the particle, where distinct compression of the lipid tails can be seen. This could be thought of as a local "puckering" of the lower leaflet lipids (see Figure 5A, 300 ns). As before, the MD simulations were then quantitatively analyzed, using the same approach as used for DOPC to compare the two systems.

In general, the data revealed that the AuNP was unable to translocate past the upper leaflet headgroups of the DPPC SLB. The citrate molecules underwent significantly less displacement, and adsorption of DPPC lipids was curtailed compared to that with the DOPC system (cf. Figure 4 and Figure 5). The vertical position of the citrate-capped AuNP relative to the DPPC SLB calculated from the CoM (solid yellow line) and outer radius (dashed yellow line, top and bottom) of the particle as a function of time was largely invariant (see Figure 5B). The position of the particle remained relatively stationary in the z-plane for the majority of the simulation, with the CoM of the AuNP never passing the trimethylamine functional groups of the DPPC upper leaflet. These data suggest that the AuNP is not fully internalized but strongly adsorbed to the DPPC SLB, unlike what was observed for DOPC. The inability of the AuNP to successfully incorporate past the upper leaflet of the membrane is further demonstrated by the constant citrate contact rate and lack of terminal carbon contacts during the 300 ns production, as shown in Figure 5C. The inability of the AuNP to undergo adsorption into the DPPC SLB limits its ability to disassociate the citrate cap off the AuNP surface and allows the citrate contacts to remain roughly in equilibrium on the surface (after minor displacement of citrate molecules on the lower facet of the AuNP that was in contact with the DPPC SLB). Furthermore, Figure 5D shows the AuNP−lipid headgroup contacts, with a preference for trimethylamine group contacts over phosphate with the AuNP throughout the 300 ns production run. Moreover, the lipid headgroup contact is localized to the bottom quarter of the particle at all times (see Figure 5D, inset), which further show a lack of particle uptake. Together, this spatial data shows a restricted vertical diffusion, with the CoM of the AuNP never passing the trimethylamine functional groups. The simulation was run at 303.15 K and results in a solid/gel phase for the membrane system and thus a lack of lateral DPPC diffusion is exhibited. The lack of adsorption is further demonstrated via the minimal contact area displayed between the AuNP and the DPPC SLB, as the AuNP cannot penetrate the membrane resulting in the low contact area, as shown in Figure 5E.

Structural assessment of the AuNP−DPPC SLB system revealed distinct differences compared to the DOPC system (cf. Figure 4E−G and Figure 5E−G). Here, the citrate-capped AuNP did not significantly alter the overall membrane lipid structure and mechanics of the membrane system as demonstrated via lipid surface-normal density (Figure 5F) and the S_{cd} (Figure 5G). This is not surprising given the lack of AuNP uptake within the bilayer, although the adsorption of the lipid headgroups and lower leaflet puckering did show a small difference in bending angle of the lipids within the SLB. Figure 5F shows the lipid density of the equilibrated mica−DPPC versus the final 10 ns membrane density. Here, the AuNP adsorption was found to have a negligible effect on the overall lipid density, due to the low adsorption depth of the AuNP. The inability of the AuNP to translocate through the DPPC membrane system reduces the AuNP impact on the overall structure and lipid mechanics of the membrane system. As such, the adsorption has more subtle effects on the overall density and lipid carbon chain structure of the membrane.

The atomic trajectory and AuNP z-diffusion profiles of DOPC versus DPPC show distinct differences in their overall adsorption dynamics of the AuNP−citrate complex at the SLB

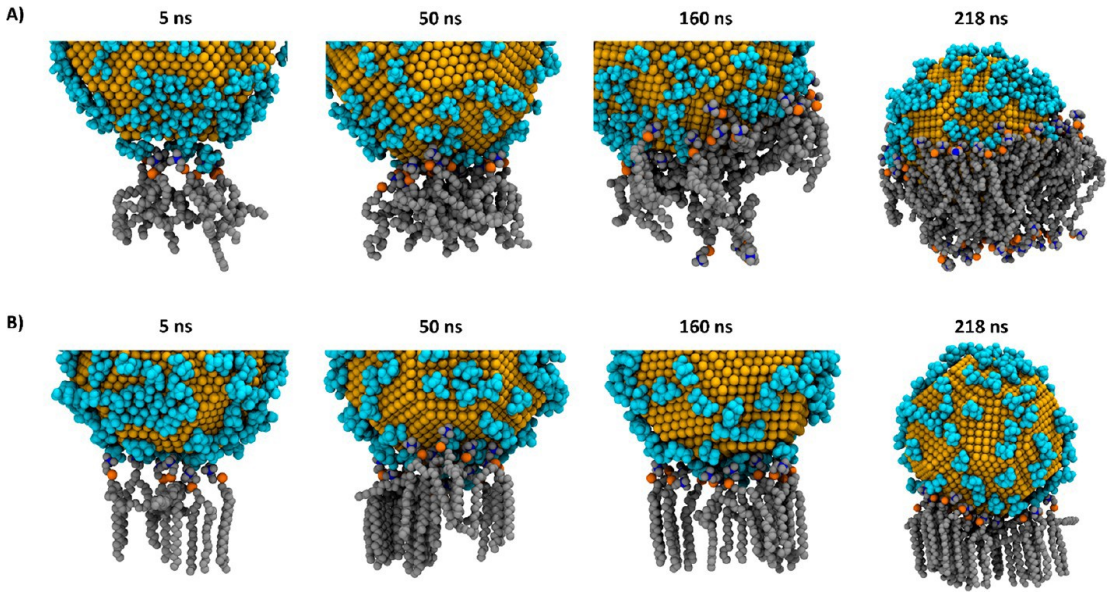

Figure 6. Closeup view of AuNP−lipid contacts during absorption/adsorption with (A) DOPC and (B) DPPC as a function of time.

interface (cf. Figure 4A,G and Figure 5A,G). The observed differences in adsorption depth can potentially be attributed to the differences in phase possessed by each membrane as their phase is also a measure of their potential intermolecular movement and therefore also contributes to particle movement resistance through the membrane. The lipid phase also defines the membranes lateral lipid diffusion coefficient. DPPC, which is in gel phase at 303.15 K, has a reported diffusion coefficient of 0.006−0.1 $\mu m^2\ s^{-1}$.[80,81] Meanwhile DOPC, which is liquid phase at 303.15 K, has a diffusion coefficient value of 1−10 $\mu m^2\ s^{-1}$.[77−79] This is consistent with the lower lateral diffusion of the AuNPs observed in the time-lapse AFM experiments for DPPC (see Figure 3) when compared to DOPC (see Figure 2).

Comparing the Local NP−Lipid Interactions. In general, particle uptake appears to be determined by the type (phase) of lipid bilayer (see Figures 4 and 5), and the subsequent degree of AuNP uptake can modulate the structure of the SLB. It was observed that the AuNP was able to change the overall lipid density of the DOPC system via volume displacement of the lipids or the surface attraction effects of the lipid molecules to the AuNP. Conversely, the inability of the AuNP to incorporate past the upper leaflet headgroups of the DPPC membrane significantly reduces the effects of the particle on the overall lipid structure within the DPPC bilayer. In DOPC, the absorption occurs in four distinct phases (Figure 6A): (1) initial attraction between the positively charged trimethylamine headgroups of DOPC and the negatively charged citrate adsorbed to the AuNP; (2) direct contact between the trimethylamine groups and the AuNP, which also brings the negatively charged phosphate groups of DOPC close to the AuNP, repelling the citrate; (3) direct contact between the lipid tails, including the terminal carbons, and the AuNP; and (4) irreversible AuNP uptake. Phase (1) involves initial displacement of the citrate cap leading to direct contact between the AuNP and lipid headgroups. While phases (1) and (2) involve electrostatic interactions, the driving force is still largely hydrophobic. The trimethylamine group has a net charge of +1*e*, but this charge is distributed across the group, and each individual methyl group retains a significant hydrophobic character and thus interacts more favorably with the AuNP than the citrate cap. Indeed, in simulations without the citrate cap, the AuNP penetrates the membrane far more quickly (Figure S17), indicating that initial electrostatic attraction between citrate and lipid headgroups is not essential for absorption. Phase (3) occurs around ~125 ns in the simulation (Figure 4) and represents the point where irreversible AuNP penetration occurs. Interestingly, just before this point, there is a slight spike in both citrate and DOPC trimethylamine contact (Figure 4C,D) coupled with a decrease in overall AuNP−DOPC contact area (Figure 4E). This is due to the rearrangement of DOPC in contact with the AuNP and rise of lipid tail contact with the AuNP, including the DOPC terminal carbons (Figure 4C). In phase (4), following contact between the AuNP and DOPC terminal carbons (from both leaflets), trimethylamine contacts decrease initially before reaching a steady value, phosphate contacts increase and even exceed trimethylamine contacts, AuNP−citrate contacts decrease steadily, and overall AuNP−DOPC contact area increases steadily until all reach equilibrium values at ~250−300 ns. The fact that trimethylamine contacts decrease and are exceeded by phosphate contacts at equilibrium demonstrates that the trimethylamine groups are not entirely hydrophobic in character and oscillate freely between contact with the AuNP, water, and other lipid headgroups, while the lipid tails remain in continuous contact with the AuNP.

In contrast, with the DPPC SLB phases (1) and (2) still occur, but the rearrangement required to allow the DPPC tails to achieve significant contact with the AuNP and initiate phase (3) is not possible, and the AuNP remains adsorbed at the interface rather than absorbed into the membrane (cf. Figure 6A and 6B). Coarse-grained simulations of citrate-capped AuNPs with free-floating DPPC membranes[82] suggest that for absorption to occur on a DPPC SLB, a substantial portion of the membrane would need to be lifted off the mica to expose the lipid tails to the AuNP, which would be highly energetically unfavorable in a SLB system.

Overall, the MD simulations revealed the general adsorption dynamics of a 5 nm citrate-coated AuNP both in a DOPC SLB and DPPC SLB. Primarily, the MD results revealed the interplay between the AuNP surface, the citrate complex, and the DOPC/DPPC lipid headgroups, highlighting the lipid-phase-dependent

adsorption process of the AuNP that was also observed within AFM experimentation. The increased inclusion of the AuNP in the DOPC SLB versus the DPPC SLB during AFM characterization was also observed within the MD simulation, and this increased inclusion was also shown to have a higher mechanical disturbance in the DOPC SLB in both the AFM and MD results. This method uses MD simulations to complement experimental AFM biophysical experiments. Additionally, these MD methods can be used for further analysis of other AFM bio-nano interaction investigations to characterize other atomistic mechanisms between different ligand coated nanoparticles and SLBs.

In this work, we show that the adsorption of citrate-capped AuNPs to SLBs is a complex process and directed by both the particle-ligand-capping agent and the underlying bilayer phase. Specifically, in our work, the citrate-capped AuNPs were capable of translocating into the interstitial spacing of the DOPC SLB, whereas the AuNP underwent only partial uptake in the DPPC SLB. In all cases, the degree of uptake was linked to AuNP ligand exchange with the lipid molecules, the extent of which was controlled by the lipid phase (see Figures 4 and 5). MD simulations showed structural changes in both systems, which included higher localized ordering of the lipids in contact with the AuNP (for DOPC). This leads to a localized stiffening of the membrane (see Figures 4 and 5). In contrast, AFM force measurements show an overall decrease in SLB cohesion when citrate-capped AuNPs were introduced, observed as a decrease in the required rupture force (see Figures 2B and 3B). This can be rationalized as a function of length scale: localized ordering of the lipid bilayer leads to generalized disorder. Further, AuNP clusters are present experimentally (see Figure S18), which likely causes further distortion of the SLB. Indeed, inspection of both MD simulations shows rearrangement of the lipids further away from the AuNP, which at larger length scales would lead to decreased order in the bilayer. The important observation is that the citrate-capped AuNP diffused slower in DPPC than for DOPC (see Figures 2 and 3), and vice versa, and these measurements should be taken as qualitatively comparative. This result is aligned with the known differences in diffusion dynamics of DOPC and DPPC. It should be noted while the AuNP inclusion in the DOPC system caused localized lipid ordering and slight membrane welling effects (due to local lipid attraction to the upper facet of the AuNP), even without the complete inclusion the AuNP, it was still able to illicit movement of the lipid molecules. The AuNP inclusion in the DPPC SLB distorted the membrane vertically (i.e., buckling) due to local interactions, and lipids begin to fill the space underneath the zone of buckling, causing a partial bulging effect on the membrane. Furthermore, there is potential for this buckling effect to cause membrane "scarring" or deformations.[83−86] Computationally, the formation of membrane pores onto free-floating membranes has been partially explored, while effects of distortions/scarring onto SLBs have not been thoroughly investigated.[83−86] However, similar interactions may cause these membrane changes, while differences in bending curvature between SLB and vesicle systems may affect overall membrane scarring or deforming behavior.[87−89]

During AuNP interaction, the displacement and local structural changes caused by the buckling effect is more notably present in the DPPC membrane. The increased lipid velocity in the fluid-phase DOPC allows temporary structural changes to be reverted/minimized, whereas in the DPPC, the slower kinetics of the lipid molecules allows for longer persisting structural changes due to lower self-assembly rate and rotational freedom of the carbon tails. The observed differences in systematic structural changes between the DOPC SLB and DPPC SLB during particle adsorption could potentially explain a potential mechanism of biocompatibility/toxicity, tailoring this factor could enhance their functionality. The successful incorporation into the fluid phase without significant membrane deformation (aside from localized lipid ordering on AuNP surface) may indicate potential biocompatibility (however, the overall unlocalized destabilizing effects are still present as well as the localized welling effects); whereas the temporary buckling effects observed in the gel phase, along with the slower self-assembly rate (lipid velocity) causing significant overall structural changes to persist within the membrane causing the membrane to distort past its natural limit, could give rise to effects such as membrane leakage, cell lysis, and intracellular water/ion penetration.[89,90] Tailoring the extent of particle adsorption via modulation of ligand, specificity to lipid domains phase, or phase-specific proteins will also allow for modulation of lipid mechanical features, cell function, and morphology as well as particle location and behavior.[91] MD simuluations revealed that the AuNP is still able to destabilize the DPPC membrane but has alternative mechanisms dependent on the lipid phase (see Figure 6). These observations can potentially explain the difference in measured rupture force found via AFM in both systems (Figures 2B and 3B), despite differences in overall penetration depth (Figures 2C and 3C, insets). The increased inclusion of the AuNP in the DOPC SLB gives rise to higher lipid carbon tail interactivity between the AuNP and causes a majority of its destabilizing effects laterally, while the increased interfacial activity of the AuNP in the DPPC SLB causes most of its destabilizing effects vertically. The generalized movement of the SLBs during AuNP interaction revealed via the MD simulations gives a reason to why the calculated rupture force, even with the reduced adsorption of the AuNP into the DPPC, showed similar destabilization of the membrane (compared to DOPC) as characterized by the comparable lowered rupture forces. It is important to note that both mechanisms of particle interaction give rise to longer lasting structural changes which destabilize the bilayer, lowering its rupture force.

Future therapies may be able to counteract the destabilizing effect of AuNPs on membranes via addition of biomolecules, lipid conjugators, polymers, etc.,[92] while also keeping the AuNP functionality and desired penetration depths via ligand/biomolecule modification.[46,93,94] The variable control of the temporary destabilizing effects of AuNP membrane inclusion may be used to enhance immunotherapies by allowing modulation of membrane stability for pharmaceutical uptake of gene therapies or nonlipophilic drugs.[95,96]

The inability of the AuNP to successfully embed completely within the gel-phase bilayer (i.e., interfacial interaction) has potential implications for other hard−soft matter or lipid−NP interactions and other biological−bilayer interactions, as other materials with similar properties may exhibit similar behavior. The ability of the AuNP to localize within the central core of the fluid-phase bilayer has potential applications in targeting specific membrane embedded protein anchorage motifs (i.e., nonpolar/hydrophobic regions of proteins).[97,98] Specificity of these domains and functionality can be further enhanced via AuNP−protein/peptide conjugation,[99−102] while cell penetration can be enhanced via alteration of ligand coating and conjugation to cell-penetrating peptides.[103] The ability of the

AuNP to potentially translocate across the gel-phase bilayer upper leaflet surface allows it to potentially illicit effects and/or delivery compounds to the cell without direct interference with intracellular organelles or other cellular constituents. Due to the various lipid domains found naturally on the cell, both internalization and interfacial surface adsorption have various widespread biomedical niches, the process of which is dictated by ligand−lipid dynamics upon the nanomaterial. Diseased cellular states relating to specific lipids, as well as other biomarkers which can be selected for (e.g., cancer cells), and are known to upregulate their fluid- or gel-phase lipids to alter their cellular proliferation, migration, metabolism, and so on.[104,105] Therefore, the ability of preferential adsorption/uptake dependent on phase, which can be further tailored with the addition of ligands and biological conjugates (peptides, antibodies, liposomes), allows for selectivity in regards to targeting of specific cellular diseased states. Being able to track the atomistic dynamics of particle movement in these systems occurring during interaction at the cellular interface is essential in more accurate design of these therapies.

Experimentally, a number of studies have documented the adsorption behavior of AuNPs, with a variety of sizes, onto solution-based bilayer interfaces, such as giant unilamellar vesicles (GUVs)[106,107] and SUVs.[43,83,84] Largely, these studies have used optical microscopy,[106] scattering techniques,[82] electron microscopy (including cryo-EM),[43,83,84] and/or spectroscopic techniques[108] to elucidate the influence of AuNP−particle adsorption on the lipid bilayer interface. In general, these studies have shown that structural changes in the lipids within the bilayer occur during adsorption, which has largely been rationalized using biophysical models.[47,84,108−110] However, these experiments often preclude investigation of ultrasmall nanoparticles, such as those investigated here, and consider only the bending of the lipid bilayer rather than particle translocation. In particular, recent cryo-EM and theoretical work by Contini et al.[84] investigated the size-dependent adsorptive behavior of citrate-capped AuNPs at the interface of DOPC and 1-palmitoyl-2-oleoyl-*sn*-glycero-3-phosphocholine (POPC) GUVs in solution. Their work noted a size-dependent adsorption, whereby smaller particles, such as 5 nm and 10 nm, were spontaneously engulfed and created distinct pores or "tubulations" within the vesicle structure, while larger particles could bend GUV membranes but were excluded from this process. Cardellini et al.[82] built on this and investigated the kinetics of adhesion of citrate-capped AuNPs onto a variety of lipid vesicles of different rigidities via a combination of light and energy scattering techniques and course-grained MD simulations. In their work, a multistep process of particle absorption was proposed, whereby particles adsorb, release citrate, embed, and induce stiffness-dependent membrane wrapping, which is dictated by the native lipid phase (soft/fluid or rigid/gel). This process was observed to lead to differential particle behavior at the liposomal interface, which was dictated by the lipid-phase cluttering on soft membranes (DOPC) or separate, bridged adhesion on rigid membranes (DPPC).[82] Together, these studies also showed how AuNP inclusions affect the lipid ordering around the particle; furthermore, it was shown that DOPC is more responsive to phase changes over DPPC, similar to the systems studied in this work.[111−113] Computationally, similar observations have been made and outlined in several studies, highlighting the adsorption process onto solution-based bilayer interface and incorporation of the AuNP within the bilayer upper leaflet and central core.[54,82,111,112,114,115]

In line with our systems, an earlier SLB computational study by Lin et al.[37] characterized the adsorption behavior at the interface of gel-phase SLB and a bare 10 nm AuNP using a CG Martini model and have found similar upper leaflet/central core localization of the AuNP, while mentioning the ability of the AuNP to elicit ordering changes of the membrane carbon tails. More recently, Wang et al.[38] attempted to understand the ligand exchange process at the fluid-phase SLB interface when interacting with 13 nm citrate-capped AuNPs and similarly have found that the adsorption process was driven by the ligand exchange mechanism, which was similar to that observed in our SLBs. Overall, the results here are in line with existing knowledge of AuNP adsorption, AuNP citrate surface exchange, membrane inclusion, lipid structural changes, and how the interplay between these drives adsorption mechanisms. Although there is a fair comparison to free-standing model membranes,[71,116−122] and experimental SLBs, the lack of other comparable computational SLB studies highlights the need for further computational analysis onto these specific systems. However, the work of Pfeiffer et al.[115] should be highlighted, as it stands as a prime, recent example of combining both experimental and computational methods to characterize the SLB interface. It should be noted, however, the use of free-standing membranes in their simulation methods. Gupta et al.[112] has also shown via molecular dynamics that incorporation and internalization past the upper leaflet into the central core (hydrophobic carbon tail region) of a 5 nm AuNP into an unsupported POPC bilayer was possible using a coarse grain Martini force field model. They also mention that a decrease in nanoparticle size (from 5 to 1 nm) was related to an increase in particle penetration, such as mentioned by Contini et al.[84,112]

CONCLUSIONS

In this work, we used a combination of AFM and MD to characterize the adsorption behavior of citrate-coated AuNPs at both fluid-phase (DOPC) and gel-phase (DPPC) SLBs with atomic resolution. Overall, both the AFM and MD results showed increased inclusion of the AuNP in the DOPC versus the DPPC bilayer, resulting in a higher degree of interaction between the membrane and the surface of the AuNP. This in turn led to greater changes in the mechanical stability of the DOPC versus the DPPC. The MD simulations were able to reveal the citrate exchange dynamics during the adsorption process and showed how the displacement of the citrate molecules by the lipid headgroups facilitated the adsorption of the AuNP into the membrane. These results explain the observed biophysical experimental AFM phenomena via atomistic computational methods. The AuNP can exert greater mechanical changes to fluid-phase membranes due to increased inclusion, and the citrate capping has a role in the overall adsorption process. However, there is a difference in the overall "fate" of the AuNP as free-standing membranes have been observed to allow greater AuNP translocation through the membrane. Current computational work on SLBs remains in its infancy, in part due to the collective favoring of free-standing models and the specific niche of creating SLB systems for computational use (as these are mostly made to compare to experimental results), where in the case of experimental systems they are routinely synthesized for AFM analysis. Currently, there is a lack of computational SLB studies and an even greater scarcity of combined AFM/MD SLB studies. As each system varies in its membrane composition, particle composition and molecular dynamics parameters, there exists a great deal of

uncategorized ligand-coated AuNP SLB interactions left to be systematically investigated.

This research illustrates how MD results can support SLB AFM results and vice versa, and when used in conjunction, these tools provide a more robust characterization of the molecular mechanism of interactions for the analysis of membrane processes. We encourage others to take a similar combined approach to their MD or AFM research for more accurate understanding of the dynamics at play. The MD structural optimization (inclusion of the mica, removal of potassium constraints, and addition of the solvation layer) along with force field parameter modulation for the AuNP can be utilized to uncover other in situ AuNP SLB model adsorption dynamics. More importantly, the observed data are currently in line with known AuNP−citrate membrane behavior. The insights gained here into the molecular mechanics of AuNP SLB adsorption will also help inform the more rational design of AuNP therapeutics. This study thus serves as a platform for further investigations.

METHODS

Lipid Preparation. Lipid solutions were prepared for AFM via the following protocol. DOPC or DPPC lipids (Avanti Polar Lipids Inc., AL, USA) were rehydrated into ultrapure Milli-Q water to a concentration of 1 mg/mL. The solutions were then bath-sonicated at 55 °C for 30 min and subjected to a freeze−thaw cycle (chilled to −20 °C for 30 min and then bath-sonicated again). At this stage, solutions appeared uniformly "milky", which is known to indicate the formation of multilamellar vesicles.[40] The solution was then extruded at least 21 (but always an odd number) times using a Mini-Extruder kit (Avanti Polar Lipids Inc., AL, USA) with a 200 nm filter membrane (Avanti Polar Lipids Inc., AL, USA). This process forms small, unilamellar vesicles (SUVs). The solution was then diluted with 150 mM NaCl to a concentration of 0.01 and 0.1 mg/mL, dependent on the experiment. All glassware and components were cleaned thoroughly by sonication with ultrapure water, then isopropyl alcohol, and water again for 10 min each prior to use.

Atomic Force Microscopy. The supported lipid bilayers were formed for surface-based investigations via self-assembly via vesicle-fusion at a freshly cleaved (refreshed) mica (muscovite) interface.[19,41,42] In brief, the respective solutions were pipetted onto a freshly cleaved mica substrate and left to equilibrate for 20 min prior to imaging. This facilitates spontaneous fusion of SUVs to the mica susbtrate.[19,41,42] This process formed either SLBs or SLBPs, depending on the concentration, high or low, respectively. Each system was studied using a Cypher ES atomic force microscope (Oxford Instrument, Asylum Research, Santa Barbara, CA, USA) at room temperature (25 °C) using AM-AFM. All images and force data were obtained using BioLever Mini BL-AC40TS cantilevers (Oxford Instrument, Asylum Research, Santa Barbara, CA, USA, nominal spring constant k_c = 0.09 N/m). To minimize the imaging force, a set point ratio (imaging amplitude (A)/free amplitude (A_0)) of >0.7−0.8 was maintained, which has been shown to minimize any tip−sample distortion and damage for a variety of materials.[123−127] Each cantilever was calibrated prior to use via the thermal spectrum method. Liquid experiments were completed in a droplet of lipid solution. This droplet was exposed to the atmosphere within an acoustic isolation cabinet (a sealed enclosure).

Figure S19 shows a model of the crystal structure of the mica surface, which is used as the bilayer support in these experiments, from the side and top perspective, respectively. Mica (muscovite) is a layered silicate, which upon basal plane cleavage, along the weak interplane potassium layer, exposes an atomically smooth, array of SiO_4 tetrahedra which form a repeating hexagonal lattice with ∼50% of the potassium left attached to the exposed plane. The dominant lattice spacing, ring center-to-ring center, is 0.52 nm.[69] Figure S19C shows a 15 nm × 15 nm AM-AFM image of the mica interface obtained within a solution of 150 mM NaCl, which is the aqueous solution used for all experiments reported. Importantly, the images appear markedly different to that of the DES−mica interface. Here, at both magnifications, a distinct hexagonal repeat structure is observed with a periodicity of 0.5 ± 0.02 nm, measured via section and 2D fast Fourier transform analysis. Side view and basal plane (without potassium ions) reconstructions of the crystal structure of the mica surface are shown in Figure S19A,B. Here, the characteristic hexagonal lattice structure is highlighted. The AFM images obtained reflect this structure, meaning that the AFM was capable of imaging the mica lattice with near-atomic resolution and provided confidence in the ability of AM-AFM to probe nanoscale phenomena with near molecular resolution (Figure S19C).

DLS Characterization. DLS experiments were performed on an ALV-5022F light scattering spectrometer equipped with a laser wavelength of 633 nm. Measurements were taken in a cylindrical glass cuvette (inner diameter: 8 mm) (LSI Instruments, Fribourg) held in a scattering vat at room temperature.

TEM Characterization. TEM images were acquired using a JEOL JEM-2100 FEGTEM microscope (JEOL, Musashino, Akishima, Tokyo, Japan) equipped with a Gatan Orius SC1000 CCD camera and operated at an acceleration voltage of 200 keV. Images were processed and analyzed using Digital Micrograph 2.31.

Molecular Dynamics Simulations. The 10 nm × 10 nm structure of the mica was adapted from our previous work.[128,129] The 5 nm AuNP was constructed using the Wulff Construction function of CHARMM-GUI Nanomaterial Modeler,[130−132] with a 2.5 nm radius and Miller indices 100, 110, and 111. The 10 nm × 10 nm DOPC and DPPC membranes were constructed using the Membrane Builder of CHARMM-GUI.[133]

Citrate was equilibrated around the AuNP in a 10 × 10 × 10 nm^3 box containing 1 AuNP and 500 citrate ions solvated in 150 mM NaCl for 100 ns, with citrate within 0.5 nm of the AuNP retained. Each complete system was composed of a 1 nm thick complete layer of mica (10 nm^2 laterally), a solvation layer to include appropriate in situ membrane dynamics,[72−74] 288 lipid molecules, the AuNP of 5743 gold atoms and 157 citrate molecules,[50] solvated in a CHARMM TIP3P water box with 0.15 M NaCl and appropriate counterions. Simulations were run using the MD code GROMACS 2020.[134] Several adjustments to the baseline model structures files and force field parameters were made to match known literature SLB behavior, including the removal of the potassium position restraints on the mica surface to allow disassociation of K^+ ions in solution,[135,136] and the modulation of the Au-epsilon (ε) parameter to a value of 3.5 for all pairwise interactions (except Au−Au) to accurately represent literature citrate surface coverage values (additional discussion in Supporting Information; see Figure S20 and Table S1).[50] Analogous procedures were used to tune Au−citrate interactions for coarse-grained force fields[82] and self-assembled monolayers on gold.[46] The INTERFACE-CHARMM force field was applied to all atoms.[137−139] Although more recently developed water models provide better reproduction of bulk properties of water,[140] we retain the use of the CHARMM TIPS3P water model here for compatibility with the CHARMM membrane model and INTERFACE-CHARMM nanomaterials. Topologies and force field parameters for the singly deprotonated citrate ions were assigned using ParamChem 2.4.0 CGenFF 4.4.[141−143]

Short-range nonbonded interactions were treated using the Verlet cutoff scheme at a distance of 1.2 Å and a switch distance of 1.0 Å, which allows a smooth truncation of the van der Waals potential energy, allowing it to approach zero slowly as the distance increases, avoiding artifacts. Long-range Coulomb interactions were calculated via the particle mesh Ewald method at a distance beyond 1.2 Å. The reference temperature during equilibration was 303.15 K and was controlled via the Berendsen temperature coupling algorithm. Temperature during production run was 303.15 K and was controlled via Nose−Hoover weak coupling dynamics allowing for an NVT ensemble. A wall was implemented in the z dimension to prevent periodic self-interactions. A time step of 2 fs was used with atomic coordinates saved every 10 ps. After the SLB systems (DOPC−mica and DPPC−mica) were run in isolation for 100 ns to reach thermal equilibrium, the 5 nm AuNP−citrate complex was added and run in triplicate for an additional 300 ns. All other simulation settings not listed here were the default settings generated by CHARMM-GUI.

The primary analysis of the thermodynamic and physical properties of the membrane−nanoparticle system was achieved via the use of GROMACS gmx analysis tools, MEMBPLUGIN[144] in VMD,[145] and FATSliM.[146] The main characteristics analyzed were the AuNP *z*-diffusion, lipid carbon chain order parameters (S_{cd}), AuNP−citrate, carbon and headgroup contacts, AuNP contact area, and lipid density function. Secondary characteristics were also analyzed and are included in the Supporting Information, such as root means squared deviation for particle diffusion, area per lipid, membrane thickness, lipid interdigitation, radial distribution, and solvent-accessible surface area.

ASSOCIATED CONTENT

Supporting Information

The Supporting Information is available free of charge at https://pubs.acs.org/doi/10.1021/acsnano.2c07751.

Additional methods and material information, schematic of SLB and SLBP formation, AuNP characterization and sizing, supporting AFM images, additional calculations, supporting force curve data, control simulation snapshots, radial distribution function data from the simulations, supporting simulation analysis, crystal structure of the mica substrate, a high-resolution AFM image of the bare mica surface, and simulation parametrization (PDF)

Movie S1 (MP4)

Movie S2 (MP4)

AUTHOR INFORMATION

Corresponding Authors

Andrew J. Christofferson − *School of Science, STEM College, RMIT University, Melbourne, VIC 3001, Australia; ARC Centre of Excellence in Exciton Science, School of Science, RMIT University, Melbourne, VIC 3001, Australia;* orcid.org/0000-0003-0904-6630; Email: andrew.christofferson@rmit.edu.au

Aaron Elbourne − *School of Science, STEM College, RMIT University, Melbourne, VIC 3001, Australia;* orcid.org/0000-0002-4472-4372; Email: aaron.elbourne@rmit.edu.au

Authors

Rashad Kariuki − *School of Science, STEM College, RMIT University, Melbourne, VIC 3001, Australia*

Rowan Penman − *School of Science, STEM College, RMIT University, Melbourne, VIC 3001, Australia*

Saffron J. Bryant − *School of Science, STEM College, RMIT University, Melbourne, VIC 3001, Australia;* orcid.org/0000-0002-7202-3004

Rebecca Orrell-Trigg − *School of Science, STEM College, RMIT University, Melbourne, VIC 3001, Australia*

Nastaran Meftahi − *ARC Centre of Excellence in Exciton Science, School of Science, RMIT University, Melbourne, VIC 3001, Australia;* orcid.org/0000-0003-2664-4368

Russell J. Crawford − *School of Science, STEM College, RMIT University, Melbourne, VIC 3001, Australia*

Chris F. McConville − *School of Science, STEM College, RMIT University, Melbourne, VIC 3001, Australia; Deakin University, Geelong, VIC 3220, Australia;* orcid.org/0000-0003-1040-2794

Gary Bryant − *School of Science, STEM College, RMIT University, Melbourne, VIC 3001, Australia;* orcid.org/0000-0001-5483-7592

Kislon Voïtchovsky − *University of Durham, Physics Department, Durham DH1 3LE, United Kingdom;* orcid.org/0000-0001-7760-4732

Charlotte E. Conn − *School of Science, STEM College, RMIT University, Melbourne, VIC 3001, Australia;* orcid.org/0000-0002-3362-3453

Complete contact information is available at: https://pubs.acs.org/10.1021/acsnano.2c07751

Notes

The authors declare no competing financial interest.

ACKNOWLEDGMENTS

A.E. is supported by an Australian Research Council (ARC) Discovery Early Career Research Award (DECRA) (DE220100511). This research was undertaken using the LIEF HPC-GPGPU Facility (Resource Grant pRMIT0013) hosted at the University of Melbourne, which was established with the assistance of LIEF Grant LE170100200. The research was also supported by computational resources provided by the Australian Government through the National Computational Infrastructure (NCI), under the National Computational Merit Allocation Scheme (Project kl59 and Resource Grant uo96).

REFERENCES

(1) Lolicato, F.; Joly, L.; Martinez-Seara, H.; Fragneto, G.; Scoppola, E.; Baldelli Bombelli, F.; Vattulainen, I.; Akola, J.; Maccarini, M. Nanoparticle-Membrane Interactions: The Role of Temperature and Lipid Charge on Intake/Uptake of Cationic Gold Nanoparticles into Lipid Bilayers (Small 23/2019). *Small* 2019, *15* (23), 1970124.

(2) Drasler, B.; Vanhecke, D.; Rodriguez-Lorenzo, L.; Petri-Fink, A.; Rothen-Rutishauser, B. Quantifying nanoparticle cellular uptake: which method is best? *Nanomedicine* 2017, *12* (10), 1095−1099.

(3) Foroozandeh, P.; Aziz, A. A. Insight into Cellular Uptake and Intracellular Trafficking of Nanoparticles. *Nanoscale Res. Lett.* 2018, *13* (1), 339−339.

(4) Niu, J.; Chu, Y.; Huang, Y.-F.; Chong, Y.-S.; Jiang, Z.-H.; Mao, Z.-W.; Peng, L.-H.; Gao, J.-Q. Transdermal Gene Delivery by Functional Peptide-Conjugated Cationic Gold Nanoparticle Reverses the Progression and Metastasis of Cutaneous Melanoma. *ACS Appl. Mater. Interfaces* 2017, *9* (11), 9388−9401.

(5) Anirudhan, T. S.; Nair, S. S. Gold Nanoparticle and Hydrophobic Nanodiamond Based Synergistic System: A Way to Overcome Skin Barrier Function. *Bioconjugate Chem.* 2018, *29* (10), 3262−3272.

(6) Sokolova, V.; Mekky, G.; van der Meer, S. B.; Seeds, M. C.; Atala, A. J.; Epple, M. Transport of ultrasmall gold nanoparticles (2 nm) across the blood-brain barrier in a six-cell brain spheroid model. *Sci. Rep.* 2020, *10* (1), 18033.

(7) Ruttala, H. B.; Ramasamy, T.; Poudel, B. K.; Ruttala, R. R. T.; Jin, S. G.; Choi, H.-G.; Ku, S.-K.; Yong, C. S.; Kim, J. O. Multi-responsive albumin-lonidamine conjugated hybridized gold nanoparticle as a combined photothermal-chemotherapy for synergistic tumor ablation. *Acta Biomaterialia* 2020, *101*, 531−543.

(8) Mao, W.; Kim, H. S.; Son, Y. J.; Kim, S. R.; Yoo, H. S. Doxorubicin encapsulated clicked gold nanoparticle clusters exhibiting tumor-specific disassembly for enhanced tumor localization and computerized tomographic imaging. *J. Controlled Release* 2018, *269*, 52−62.

(9) Kim, S.-E.; Lee, B.-R.; Lee, H.; Jo, S. D.; Kim, H.; Won, Y.-Y.; Lee, J. Near-Infrared Plasmonic Assemblies of Gold Nanoparticles with Multimodal Function for Targeted Cancer Theragnosis. *Sci. Rep.* 2017, *7* (1), 17327.

(10) Wang, Y.; Yang, Y.; Yang, L.; Lin, Y.; Tian, Y.; Ni, Q.; Wang, S.; Ju, H.; Guo, J.; Lu, G. Gold Nanostar@Polyaniline Theranostic Agent with High Photothermal Conversion Efficiency for Photoacoustic Imaging-Guided Anticancer Phototherapy at a Low Dosage. *ACS Appl. Mater. Interfaces* 2022, *14* (25), 28570−28580.

(11) Mitiche, S.; Gueffrache, S.; Marguet, S.; Audibert, J.-F.; Pansu, R. B.; Palpant, B. Coating gold nanorods with silica prevents the generation of reactive oxygen species under laser light irradiation for safe biomedical applications. *J. Mater. Chem. B* 2022, *10* (4), 589−597.
(12) Wang, H.; Liu, Y.; Yu, J.; Luo, Y.; Wang, L.; Yang, T.; Raktani, B.; Lee, H. Selectively Regulating the Chiral Morphology of Amino Acid-Assisted Chiral Gold Nanoparticles with Circularly Polarized Light. *ACS Appl. Mater. Interfaces* 2022, *14* (2), 3559−3567.
(13) Kulkarni, T.; Mukhopadhyay, D.; Bhattacharya, S. Influence of surface moieties on nanomechanical properties of gold nanoparticles using atomic force microscopy. *Appl. Surf. Sci.* 2022, *591*, 153175.
(14) Marquart, G. W.; Stoddard, J.; Kinnison, K.; Zhou, F.; Hugo, R.; Ryals, R.; Shubert, S.; McGill, T. J.; Mackiewicz, M. R. Increasing the Efficacy of Gold Nanorod Uptake in Stem Cell-Derived Therapeutic Cells: Implications for Stem Cell Labeling and Optical Coherence Tomography Imaging. *ACS Applied Nano Materials* 2022, *5* (5), 6995−7008.
(15) Oh, N.; Park, J.-H. Surface Chemistry of Gold Nanoparticles Mediates Their Exocytosis in Macrophages. *ACS Nano* 2014, *8* (6), 6232−6241.
(16) Yu, H.; Zheng, R.; Lei, F.; Wang, W.; Guo, W.; Zhang, L.; Liu, Y.; Chen, X.; Wang, Y. Antibody-conjugated silica-coated gold nanoparticles in targeted therapy of cervical cancer. *Am. J. Transl. Res.* 2022, *14* (3), 1518−1534.
(17) Mostafa, O.; Saleh, H. M.; Salaheldin, T. A.; Elfeky, S. A. Fluorescein/gold nanoparticles conjugated EGFR antibody for imaging and P53 upregulation in hamster mucosal cells carcinoma. *Journal of Drug Delivery Science and Technology* 2022, 103293.
(18) Zhigaltsev, I. V.; Tam, Y. Y. C.; Kulkarni, J. A.; Cullis, P. R. Synthesis and Characterization of Hybrid Lipid Nanoparticles Containing Gold Nanoparticles and a Weak Base Drug. *Langmuir* 2022, *38* (25), 7858−7866.
(19) Veeren, A.; Ogunyankin, M. O.; Shin, J. E.; Zasadzinski, J. A. Liposome-Tethered Gold Nanoparticles Triggered by Pulsed NIR Light for Rapid Liposome Contents Release and Endosome Escape. *Pharmaceutics* 2022, *14* (4), 701.
(20) Hu, C.-M. J.; Zhang, L.; Aryal, S.; Cheung, C.; Fang, R. H.; Zhang, L. Erythrocyte membrane-camouflaged polymeric nanoparticles as a biomimetic delivery platform. *Proc. Natl. Acad. Sci. U. S. A.* 2011, *108* (27), 10980−10985.
(21) Lerch, S.; Dass, M.; Musyanovych, A.; Landfester, K.; Mailänder, V. Polymeric nanoparticles of different sizes overcome the cell membrane barrier. *Eur. J. Pharm. Biopharm.* 2013, *84* (2), 265−274.
(22) Nicol, J. R.; Dixon, D.; Coulter, J. A. Gold nanoparticle surface functionalization: a necessary requirement in the development of novel nanotherapeutics. *Nanomedicine (Lond)* 2015, *10* (8), 1315−1326.
(23) Singh, P.; Pandit, S.; Mokkapati, V. R. S. S.; Garg, A.; Ravikumar, V.; Mijakovic, I. Gold Nanoparticles in Diagnostics and Therapeutics for Human Cancer. *International journal of molecular sciences* 2018, *19* (7), 1979.
(24) Patil, T.; Gambhir, R.; Vibhute, A.; Tiwari, A. P. Gold Nanoparticles: Synthesis Methods, Functionalization and Biological Applications. *Journal of Cluster Science* 2022, DOI: 10.1007/s10876-022-02287-6.
(25) Amina, S. J.; Guo, B. A Review on the Synthesis and Functionalization of Gold Nanoparticles as a Drug Delivery Vehicle. *Int. J. Nanomedicine* 2020, *15*, 9823−9857.
(26) Lavagna, E.; Güven, Z. P.; Bochicchio, D.; Olgiati, F.; Stellacci, F.; Rossi, G. Amphiphilic nanoparticles generate curvature in lipid membranes and shape liposome-liposome interfaces. *Nanoscale* 2021, *13* (40), 16879−16884.
(27) Kulkarni, T.; Mukhopadhyay, D.; Bhattacharya, S. Dynamic alteration of poroelastic attributes as determinant membrane nanorheology for endocytosis of organ specific targeted gold nanoparticles. *J. Nanobiotechnology* 2022, *20* (1), 74.
(28) Huang, R. H.; Nayeem, N.; He, Y.; Morales, J.; Graham, D.; Klajn, R.; Contel, M.; O'Brien, S.; Ulijn, R. V. Self-Complementary Zwitterionic Peptides Direct Nanoparticle Assembly and Enable Enzymatic Selection of Endocytic Pathways. *Adv. Mater.* 2022, *34* (1), 2104962.
(29) Vetten, M.; Gulumian, M. Differences in uptake of 14 nm PEG-liganded gold nanoparticles into BEAS-2B cells is dependent on their functional groups. *Toxicol. Appl. Pharmacol.* 2019, *363*, 131−141.
(30) Oh, N.; Park, J.-H. Endocytosis and exocytosis of nanoparticles in mammalian cells. *International journal of nanomedicine* 2014, *9* (Suppl 1), 51.
(31) Rennick, J. J.; Johnston, A. P. R.; Parton, R. G. Key principles and methods for studying the endocytosis of biological and nanoparticle therapeutics. *Nat. Nanotechnol.* 2021, *16* (3), 266−276.
(32) Sousa de Almeida, M.; Susnik, E.; Drasler, B.; Taladriz-Blanco, P.; Petri-Fink, A.; Rothen-Rutishauser, B. Understanding nanoparticle endocytosis to improve targeting strategies in nanomedicine. *Chem. Soc. Rev.* 2021, *50* (9), 5397−5434.
(33) Ridolfi, A.; Caselli, L.; Montis, C.; Mangiapia, G.; Berti, D.; Brucale, M.; Valle, F. Gold nanoparticles interacting with synthetic lipid rafts: an AFM investigation. *J. Microsc.* 2020, *280* (3), 194−203.
(34) Troiano, J. M.; Olenick, L. L.; Kuech, T. R.; Melby, E. S.; Hu, D.; Lohse, S. E.; Mensch, A. C.; Dogangun, M.; Vartanian, A. M.; Torelli, M. D.; et al. Direct Probes of 4 nm Diameter Gold Nanoparticles Interacting with Supported Lipid Bilayers. *J. Phys. Chem. C* 2015, *119* (1), 534−546.
(35) Sakaguchi, N.; Kimura, Y.; Hirano-Iwata, A.; Ogino, T. Fabrication of Au-Nanoparticle-Embedded Lipid Bilayer Membranes Supported on Solid Substrates. *J. Phys. Chem. B* 2017, *121* (17), 4474−4481.
(36) Bunga, Y.; Kataky, R. Real time monitoring of interactions of gold nanoparticles with supported phospholipid lipid layers. *J. Electroanal. Chem.* 2020, *872*, 114302.
(37) Lin, X.; Wang, C.; Wang, M.; Fang, K.; Gu, N. Computer Simulation of the Effects of Nanoparticles' Adsorption on the Properties of Supported Lipid Bilayer. *J. Phys. Chem. C* 2012, *116* (33), 17960−17968.
(38) Wang, X.; Wang, X.; Bai, X.; Yan, L.; Liu, T.; Wang, M.; Song, Y.; Hu, G.; Gu, Z.; Miao, Q.; et al. Nanoparticle Ligand Exchange and Its Effects at the Nanoparticle-Cell Membrane Interface. *Nano Lett.* 2019, *19* (1), 8−18.
(39) Xing, C.; Faller, R. Interactions of Lipid Bilayers with Supports: A Coarse-Grained Molecular Simulation Study. *J. Phys. Chem. B* 2008, *112* (23), 7086−7094.
(40) Trewby, W.; Faraudo, J.; Voïtchovsky, K. Long-lived ionic nanodomains can modulate the stiffness of soft interfaces. *Nanoscale* 2019, *11* (10), 4376−4384.
(41) Gunstone, F. D. *Fatty Acid and Lipid Chemistry*, 1st ed.; Springer: New York, NY, 2012; Vol. *XI*, p 252.
(42) Murthy, S. K. Nanoparticles in modern medicine: state of the art and future challenges. *Int. J. Nanomed.* 2007, *2* (2), 129−141.
(43) Contini, C.; Schneemilch, M.; Gaisford, S.; Quirke, N. Nanoparticle-membrane interactions. *Journal of Experimental Nanoscience* 2018, *13* (1), 62−81.
(44) Zhang, Q.; Gong, Y.; Guo, X.-j.; Zhang, P.; Ding, C.-f. Multifunctional Gold Nanoparticle-Based Fluorescence Resonance Energy-Transfer Probe for Target Drug Delivery and Cell Fluorescence Imaging. *ACS Appl. Mater. Interfaces* 2018, *10* (41), 34840−34848.
(45) Hinde, E.; Thammasiraphop, K.; Duong, H. T. T.; Yeow, J.; Karagoz, B.; Boyer, C.; Gooding, J. J.; Gaus, K. Pair correlation microscopy reveals the role of nanoparticle shape in intracellular transport and site of drug release. *Nat. Nanotechnol.* 2017, *12* (1), 81−89.
(46) Hoff, S. E.; Di Silvio, D.; Ziolo, R. F.; Moya, S. E.; Heinz, H. Patterning of Self-Assembled Monolayers of Amphiphilic Multisegment Ligands on Nanoparticles and Design Parameters for Protein Interactions. *ACS Nano* 2022, *16* (6), 8766−8783.
(47) Wang, F.; Liu, J. Self-healable and reversible liposome leakage by citrate-capped gold nanoparticles: probing the initial adsorption/desorption induced lipid phase transition. *Nanoscale* 2015, *7* (38), 15599−15604.

(48) Chong, G.; Hernandez, R. Adsorption Dynamics and Structure of Polycations on Citrate-Coated Gold Nanoparticles. *J. Phys. Chem. C* 2018, *122* (34), 19962−19969.
(49) Freese, C.; Uboldi, C.; Gibson, M. I.; Unger, R. E.; Weksler, B. B.; Romero, I. A.; Couraud, P.-O.; Kirkpatrick, C. J. Uptake and cytotoxicity of citrate-coated gold nanospheres: Comparative studies on human endothelial and epithelial cells. *Particle and Fibre Toxicology* 2012, *9* (1), 23.
(50) Chong, G.; Laudadio, E. D.; Wu, M.; Murphy, C. J.; Hamers, R. J.; Hernandez, R. Density, Structure, and Stability of Citrate3- and H2citrate- on Bare and Coated Gold Nanoparticles. *J. Phys. Chem. C* 2018, *122* (49), 28393−28404.
(51) Grys, D.-B.; de Nijs, B.; Salmon, A. R.; Huang, J.; Wang, W.; Chen, W.-H.; Scherman, O. A.; Baumberg, J. J. Citrate Coordination and Bridging of Gold Nanoparticles: The Role of Gold Adatoms in AuNP Aging. *ACS Nano* 2020, *14* (7), 8689−8696.
(52) Park, J.-W.; Shumaker-Parry, J. S. Structural Study of Citrate Layers on Gold Nanoparticles: Role of Intermolecular Interactions in Stabilizing Nanoparticles. *J. Am. Chem. Soc.* 2014, *136* (5), 1907−1921.
(53) Perfilieva, O. A.; Pyshnyi, D. V.; Lomzov, A. A. Molecular Dynamics Simulation of Polarizable Gold Nanoparticles Interacting with Sodium Citrate. *J. Chem. Theory Comput.* 2019, *15* (2), 1278−1292.
(54) Salassi, S.; Caselli, L.; Cardellini, J.; Lavagna, E.; Montis, C.; Berti, D.; Rossi, G. A Martini Coarse Grained Model of Citrate-Capped Gold Nanoparticles Interacting with Lipid Bilayers. *J. Chem. Theory Comput.* 2021, *17* (10), 6597−6609.
(55) Ghosh, A.; Sharma, A.; Chizhik, A. I.; Isbaner, S.; Ruhlandt, D.; Tsukanov, R.; Gregor, I.; Karedla, N.; Enderlein, J. Graphene-based metal-induced energy transfer for sub-nanometre optical localization. *Nat. Photonics* 2019, *13* (12), 860−865.
(56) Castellana, E. T.; Cremer, P. S. Solid supported lipid bilayers: From biophysical studies to sensor design. *Surf. Sci. Rep.* 2006, *61* (10), 429−444.
(57) Stelzle, M.; Miehlich, R.; Sackmann, E. Two-dimensional microelectrophoresis in supported lipid bilayers. *Biophys. J.* 1992, *63* (5), 1346−1354.
(58) Burns, A. R.; Frankel, D. J.; Buranda, T. Local Mobility in Lipid Domains of Supported Bilayers Characterized by Atomic Force Microscopy and Fluorescence Correlation Spectroscopy. *Biophys. J.* 2005, *89* (2), 1081−1093.
(59) Alessandrini, A.; Facci, P. Model Bio-Membranes Investigated by AFM and AFS: A Suitable Tool to Unravel Lipid Organization and their Interaction with Proteins. *Smart Membranes and Sensors* 2014, 185−226.
(60) Mingeot-Leclercq, M.-P.; Deleu, M.; Brasseur, R.; Dufrêne, Y. F. Atomic force microscopy of supported lipid bilayers. *Nat. Protoc.* 2008, *3* (10), 1654−1659.
(61) Al-Rekabi, Z.; Contera, S. Multifrequency AFM reveals lipid membrane mechanical properties and the effect of cholesterol in modulating viscoelasticity. *Proc. Natl. Acad. Sci. U. S. A.* 2018, *115* (11), 2658−2663.
(62) Reitsma, S.; Slaaf, D. W.; Vink, H.; van Zandvoort, M. A. M. J.; oude Egbrink, M. G. A. The endothelial glycocalyx: composition, functions, and visualization. *Pflügers Archiv-European Journal of Physiology* 2007, *454* (3), 345−359.
(63) Weinbaum, S.; Tarbell, J. M.; Damiano, E. R. The structure and function of the endothelial glycocalyx layer. *Annu. Rev. Biomed. Eng.* 2007, *9*, 121−167.
(64) Montis, C.; Caselli, L.; Valle, F.; Zendrini, A.; Carlà, F.; Schweins, R.; Maccarini, M.; Bergese, P.; Berti, D. Shedding light on membrane-templated clustering of gold nanoparticles. *J. Colloid Interface Sci.* 2020, *573*, 204−214.
(65) Lochbaum, C. A.; Chew, A. K.; Zhang, X.; Rotello, V.; Van Lehn, R. C.; Pedersen, J. A. Lipophilicity of Cationic Ligands Promotes Irreversible Adsorption of Nanoparticles to Lipid Bilayers. *ACS Nano* 2021, *15* (4), 6562−6572.
(66) Miller, E. J.; Voïtchovsky, K.; Staykova, M. Substrate-led cholesterol extraction from supported lipid membranes. *Nanoscale* 2018, *10* (34), 16332−16342.
(67) Marrink, S.-J.; Berger, O.; Tieleman, P.; Jähnig, F. Adhesion Forces of Lipids in a Phospholipid Membrane Studied by Molecular Dynamics Simulations. *Biophys. J.* 1998, *74* (2), 931−943.
(68) Tae, H.; Park, S.; Kim, S.-O.; Yorulmaz Avsar, S.; Cho, N.-J. Selective Recognition of Phosphatidylinositol Phosphate Receptors by C-Terminal Tail of Mitotic Kinesin-like Protein 2 (MKlp2). *J. Phys. Chem. B* 2022, *126* (12), 2345−2352.
(69) Attwood, S. J.; Choi, Y.; Leonenko, Z. Preparation of DOPC and DPPC Supported Planar Lipid Bilayers for Atomic Force Microscopy and Atomic Force Spectroscopy. *Int. J. Mol. Sci.* 2013, *14* (2), 3514−3539.
(70) Picas, L.; Rico, F.; Scheuring, S. Direct measurement of the mechanical properties of lipid phases in supported bilayers. *Biophys. J.* 2012, *102* (1), L01−L03.
(71) Dekkiche, F.; Corneci, M. C.; Trunfio-Sfarghiu, A. M.; Munteanu, B.; Berthier, Y.; Kaabar, W.; Rieu, J. P. Stability and tribological performances of fluid phospholipid bilayers: Effect of buffer and ions. *Colloids Surf., B* 2010, *80* (2), 232−239.
(72) Nissen, J.; Gritsch, S.; Wiegand, G.; Rädler, J. O. Wetting of phospholipid membranes on hydrophilic surfaces - Concepts towards self-healing membranes. *European Physical Journal B - Condensed Matter and Complex Systems* 1999, *10* (2), 335−344.
(73) Pertsin, A.; Grunze, M. Possible mechanism of adhesion in a mica supported phospholipid bilayer. *J. Chem. Phys.* 2014, *140* (18), 184707.
(74) Chattopadhyay, M.; Krok, E.; Orlikowska, H.; Schwille, P.; Franquelim, H. G.; Piatkowski, L. Hydration Layer of Only a Few Molecules Controls Lipid Mobility in Biomimetic Membranes. *J. Am. Chem. Soc.* 2021, *143* (36), 14551−14562.
(75) Rostek, A.; Mahl, D.; Epple, M. Chemical composition of surface-functionalized gold nanoparticles. *J. Nanopart. Res.* 2011, *13* (10), 4809−4814.
(76) Wei, X.; Popov, A.; Hernandez, R. Electric Potential of Citrate-Capped Gold Nanoparticles Is Affected by Poly(allylamine hydrochloride) and Salt Concentration. *ACS Appl. Mater. Interfaces* 2022, *14* (10), 12538−12550.
(77) Jan Akhunzada, M.; D'Autilia, F.; Chandramouli, B.; Bhattacharjee, N.; Catte, A.; Di Rienzo, R.; Cardarelli, F.; Brancato, G. Interplay between lipid lateral diffusion, dye concentration and membrane permeability unveiled by a combined spectroscopic and computational study of a model lipid bilayer. *Sci. Rep.* 2019, *9* (1), 1508.
(78) Lindblom, G.; Orädd, G. Lipid lateral diffusion and membrane heterogeneity. *Biochimica et Biophysica Acta (BBA) - Biomembranes* 2009, *1788* (1), 234−244.
(79) Reddy, A. S.; Warshaviak, D. T.; Chachisvilis, M. Effect of membrane tension on the physical properties of DOPC lipid bilayer membrane. *Biochimica et Biophysica Acta (BBA) - Biomembranes* 2012, *1818* (9), 2271−2281.
(80) Scomparin, C.; Lecuyer, S.; Ferreira, M.; Charitat, T.; Tinland, B. Diffusion in supported lipid bilayers: Influence of substrate and preparation technique on the internal dynamics. *Eur. Phys. J. E* 2009, *28* (2), 211−220.
(81) Hofsäss, C.; Lindahl, E.; Edholm, O. Molecular dynamics simulations of phospholipid bilayers with cholesterol. *Biophys. J.* 2003, *84* (4), 2192−2206.
(82) Cardellini, J.; Caselli, L.; Lavagna, E.; Salassi, S.; Amenitsch, H.; Calamai, M.; Montis, C.; Rossi, G.; Berti, D. Membrane Phase Drives the Assembly of Gold Nanoparticles on Biomimetic Lipid Bilayers. *J. Phys. Chem. C* 2022, *126* (9), 4483−4494.
(83) Contini, C.; Hindley, J.; Macdonald, T.; Barritt, J.; Ces, O.; Quirke, N. Size matters: Size Dependency of Gold Nanoparticles Interacting with Model Membranes. *ChemRxiv* 2019, DOI: 10.26434/chemrxiv.10246928.v1.
(84) Contini, C.; Hindley, J. W.; Macdonald, T. J.; Barritt, J. D.; Ces, O.; Quirke, N. Size dependency of gold nanoparticles interacting with model membranes. *Communications Chemistry* 2020, *3* (1), 130.

(85) Wiemann, J. T.; Shen, Z.; Ye, H.; Li, Y.; Yu, Y. Membrane poration, wrinkling, and compression: deformations of lipid vesicles induced by amphiphilic Janus nanoparticles. *Nanoscale* 2020, *12* (39), 20326−20336.
(86) Li, S.; Malmstadt, N. Deformation and poration of lipid bilayer membranes by cationic nanoparticles. *Soft Matter* 2013, *9* (20), 4969−4976.
(87) Canepa, E.; Relini, A.; Bochicchio, D.; Lavagna, E.; Mescola, A. Amphiphilic Gold Nanoparticles: A Biomimetic Tool to Gain Mechanistic Insights into Peptide-Lipid Interactions. *Membranes* 2022, *12* (7), 673.
(88) Nademi, Y.; Tang, T.; Uludağ, H. Nature of bilayer lipids affects membranes deformation and pore resealing during nanoparticle penetration. *Materials Science and Engineering: C* 2022, *132*, 112530.
(89) Fang, B.; Dai, X.; Li, B.; Qu, Y.; Li, Y.-Q.; Zhao, M.; Yang, Y.; Li, W. Self-assembly of ultra-small-sized carbon nanoparticles in lipid membrane disrupts its integrity. *Nanoscale Advances* 2021, *4* (1), 163−172.
(90) Song, B.; Yuan, H.; Pham, S. V.; Jameson, C. J.; Murad, S. Nanoparticle Permeation Induces Water Penetration, Ion Transport, and Lipid Flip-Flop. *Langmuir* 2012, *28* (49), 16989−17000.
(91) Sohrabi Kashani, A.; Larocque, K.; Piekny, A.; Packirisamy, M. Gold Nano-Bio-Interaction to Modulate Mechanobiological Responses for Cancer Therapy Applications. *ACS Applied Bio Materials* 2022, *5*, 3741.
(92) Shah, S.; Famta, P.; Raghuvanshi, R. S.; Singh, S. B.; Srivastava, S. Lipid polymer hybrid nanocarriers: Insights into synthesis aspects, characterization, release mechanisms, surface functionalization and potential implications. *Colloid and Interface Science Communications* 2022, *46*, 100570.
(93) Liu, H.; Pei, Y. Atomistic Molecular Dynamics Simulation Study on the Interaction between Atomically Precise Thiolate-Protected Gold Nanoclusters and Phospholipid Membranes. *Langmuir* 2022, *38* (5), 1653−1661.
(94) Chew, A. K.; Pedersen, J. A.; Van Lehn, R. C. Predicting the Physicochemical Properties and Biological Activities of Monolayer-Protected Gold Nanoparticles Using Simulation-Derived Descriptors. *ACS Nano* 2022, *16* (4), 6282−6292.
(95) Du, X.; Wang, J.; Zhou, Q.; Zhang, L.; Wang, S.; Zhang, Z.; Yao, C. Advanced physical techniques for gene delivery based on membrane perforation. *Drug Delivery* 2018, *25* (1), 1516−1525.
(96) Mirchandani, Y.; Patravale, V. B.; S, B. Solid lipid nanoparticles for hydrophilic drugs. *J. Controlled Release* 2021, *335*, 457−464.
(97) Zuo, G.; Huang, Q.; Wei, G.; Zhou, R.; Fang, H. Plugging into Proteins: Poisoning Protein Function by a Hydrophobic Nanoparticle. *ACS Nano* 2010, *4* (12), 7508−7514.
(98) Ren, J.; Andrikopoulos, N.; Velonia, K.; Tang, H.; Cai, R.; Ding, F.; Ke, P. C.; Chen, C. Chemical and Biophysical Signatures of the Protein Corona in Nanomedicine. *J. Am. Chem. Soc.* 2022, *144* (21), 9184−9205.
(99) Mittelheisser, V.; Coliat, P.; Moeglin, E.; Goepp, L.; Goetz, J. G.; Charbonniere, L. J.; Pivot, X.; Detappe, A. Optimal Physicochemical Properties of Antibody-Nanoparticle Conjugates for Improved Tumor Targeting. *Adv. Mater.* 2022, *34* (24), No. 2110305.
(100) Cai, X.; Chen, M.; Prominski, A.; Lin, Y.; Ankenbruck, N.; Rosenberg, J.; Nguyen, M.; Shi, J.; Tomatsidou, A.; Randall, G.; et al. A Multifunctional Neutralizing Antibody-Conjugated Nanoparticle Inhibits and Inactivates SARS-CoV-2. *Advanced Science* 2022, *9* (2), 2103240.
(101) Srivastava, I.; Xue, R.; Jones, J.; Rhee, H.; Flatt, K.; Gruev, V.; Nie, S. Biomimetic Surface-Enhanced Raman Scattering Nanoparticles with Improved Dispersibility, Signal Brightness, and Tumor Targeting Functions. *ACS Nano* 2022, *16* (5), 8051−8063.
(102) Ukidve, A.; Zhao, Z.; Fehnel, A.; Krishnan, V.; Pan, D. C.; Gao, Y.; Mandal, A.; Muzykantov, V.; Mitragotri, S. Erythrocyte-driven immunization via biomimicry of their natural antigen-presenting function. *Proc. Natl. Acad. Sci. U. S. A.* 2020, *117* (30), 17727−17736.
(103) Chiu, J. Z. S.; Castillo, A. M.; Tucker, I. G.; Radunskaya, A. E.; McDowell, A. Modeling the interaction of polymeric nanoparticles functionalized with cell penetrating peptides at the nano-bio interface. *Colloids Surf., B* 2022, *217*, 112626.
(104) Agarwala, P. K.; Aneja, R.; Kapoor, S. Lipidomic landscape in cancer: Actionable insights for membrane-based therapy and diagnoses. *Medicinal Research Reviews* 2022, *42* (2), 983−1018.
(105) Pillai, S.; Mahmud, I.; Mahar, R.; Griffith, C.; Langsen, M.; Nguyen, J.; Wojtkowiak, J. W.; Swietach, P.; Gatenby, R. A.; Bui, M. M.; et al. Lipogenesis mediated by OGR1 regulates metabolic adaptation to acid stress in cancer cells via autophagy. *Cell Reports* 2022, *39* (6), 110796.
(106) Bhat, A.; Huan, K.; Cooks, T.; Boukari, H.; Lu, Q. Probing Interactions between AuNPs/AgNPs and Giant Unilamellar Vesicles (GUVs) Using Hyperspectral Dark-field Microscopy. *International journal of molecular sciences* 2018, *19* (4), 1014.
(107) Van Lehn, R. C.; Atukorale, P. U.; Carney, R. P.; Yang, Y.-S.; Stellacci, F.; Irvine, D. J.; Alexander-Katz, A. Effect of Particle Diameter and Surface Composition on the Spontaneous Fusion of Monolayer-Protected Gold Nanoparticles with Lipid Bilayers. *Nano Lett.* 2013, *13* (9), 4060−4067.
(108) Živanović, V.; Kochovski, Z.; Arenz, C.; Lu, Y.; Kneipp, J. SERS and Cryo-EM Directly Reveal Different Liposome Structures during Interaction with Gold Nanoparticles. *J. Phys. Chem. Lett.* 2018, *9* (23), 6767−6772.
(109) Wang, F.; Curry, D. E.; Liu, J. Driving Adsorbed Gold Nanoparticle Assembly by Merging Lipid Gel/Fluid Interfaces. *Langmuir* 2015, *31* (49), 13271−13274.
(110) Bhat, A.; Edwards, L. W.; Fu, X.; Badman, D. L.; Huo, S.; Jin, A. J.; Lu, Q. Effects of gold nanoparticles on lipid packing and membrane pore formation. *Appl. Phys. Lett.* 2016, *109* (26), 263106.
(111) Mhashal, A. R.; Roy, S. Effect of Gold Nanoparticle on Structure and Fluidity of Lipid Membrane. *PLoS One* 2014, *9* (12), No. e114152.
(112) Gupta, R.; Rai, B. Effect of Size and Surface Charge of Gold Nanoparticles on their Skin Permeability: A Molecular Dynamics Study. *Sci. Rep.* 2017, *7* (1), 45292.
(113) Canepa, E.; Salassi, S.; Simonelli, F.; Ferrando, R.; Rolandi, R.; Lambruschini, C.; Canepa, F.; Dante, S.; Relini, A.; Rossi, G. Non-disruptive uptake of anionic and cationic gold nanoparticles in neutral zwitterionic membranes. *Sci. Rep.* 2021, *11* (1), 1256.
(114) Lin, X.; Lin, X.; Gu, N. Optimization of hydrophobic nanoparticles to better target lipid rafts with molecular dynamics simulations. *Nanoscale* 2020, *12* (6), 4101−4109.
(115) Pfeiffer, T.; De Nicola, A.; Montis, C.; Carlà, F.; van der Vegt, N. F.; Berti, D.; Milano, G. Nanoparticles at biomimetic interfaces: combined experimental and simulation study on charged gold nanoparticles/lipid bilayer interfaces. *journal of physical chemistry letters* 2019, *10* (2), 129−137.
(116) Al-Rekabi, Z.; Contera, S. Multifrequency AFM reveals lipid membrane mechanical properties and the effect of cholesterol in modulating viscoelasticity. *Proc. Natl. Acad. Sci. U. S. A.* 2018, *115*, 2658.
(117) Butt, H. J.; Cappella, B.; Kappl, M. Force measurements with the atomic force microscope: Technique, interpretation and applications. *Surf. Sci. Rep.* 2005, *59* (1−6), 1−152.
(118) Goksu, E. I.; Vanegas, J. M.; Blanchette, C. D.; Lin, W.-C.; Longo, M. L. AFM for structure and dynamics of biomembranes. *Biochimica et Biophysica Acta (BBA) - Biomembranes* 2009, *1788* (1), 254−266.
(119) Lv, Z.; Banerjee, S.; Zagorski, K.; Lyubchenko, Y. L. Supported Lipid Bilayers for Atomic Force Microscopy Studies. *Methods Mol. Biol.* 2018, *1814*, 129−143.
(120) Reviakine, I.; Brisson, A. Formation of Supported Phospholipid Bilayers from Unilamellar Vesicles Investigated by Atomic Force Microscopy. *Langmuir* 2000, *16* (4), 1806−1815.
(121) Richter, R. P.; Brisson, A. R. Following the formation of supported lipid bilayers on mica: a study combining AFM, QCM-D, and ellipsometry. *Biophysical journal* 2005, *88* (5), 3422−3433.
(122) Seantier, B.; Breffa, C.; Félix, O.; Decher, G. In Situ Investigations of the Formation of Mixed Supported Lipid Bilayers

Close to the Phase Transition Temperature. *Nano Lett.* 2004, *4* (1), 5−10.
(123) García, R. *Amplitude Modulation Atomic Force Microscopy*, 1st ed.; Wiley-VCH Verlag GmbH & Co. KGaA: Weinheim, Germany, 2010; Vol. *1*, pp 77−90.
(124) Voitchovsky, K. Anharmonicity, solvation forces, and resolution in atomic force microscopy at the solid-liquid interface. *Phys. Rev. E* 2013, *88* (2), 022407.
(125) Page, A. J.; Elbourne, A.; Stefanovic, R.; Addicoat, M. A.; Warr, G. G.; Voitchovsky, K.; Atkin, R. 3-Dimensional Atomic Scale Structure of the Ionic Liquid-Graphite Interface Elucidated by AM-AFM and Quantum Chemical Simulations. *Nanoscale* 2014, *6* (14), 8100−8106.
(126) Elbourne, A.; McDonald, S.; Voïchovsky, K.; Endres, F.; Warr, G. G.; Atkin, R. Nanostructure of the Ionic Liquid-Graphite Stern Layer. *ACS Nano* 2015, *9* (7), 7608−7620.
(127) Elbourne, A.; McLean, B.; Voïtchovsky, K.; Warr, G. G.; Atkin, R. Molecular Resolution in situ Imaging of Spontaneous Graphene Exfoliation. *J. Phys. Chem. Lett.* 2016, *7* (16), 3118−3122.
(128) Elbourne, A.; Meftahi, N.; Greaves, T. L.; McConville, C. F.; Bryant, G.; Bryant, S. J.; Christofferson, A. J. Nanostructure of a Deep Eutectic Solvent at Solid Interfaces. *J. Colloid Interface Sci.* 2021, *591*, 38−51.
(129) Elbourne, A.; Besford, Q. A.; Meftahi, N.; Crawford, R. J.; Daeneke, T.; Greaves, T. L.; McConville, C. F.; Bryant, G.; Bryant, S. J.; Christofferson, A. J. The Impact of Water on the Lateral Nanostructure of a Deep Eutectic Solvent-Solid Interface. *Aust. J. Chem.* 2022, *75*, 111.
(130) Jo, S.; Kim, T.; Iyer, V. G.; Im, W. CHARMM-GUI: A web-based graphical user interface for CHARMM. *J. Comput. Chem.* 2008, *29* (11), 1859−1865.
(131) Choi, Y. K.; Kern, N. R.; Kim, S.; Kanhaiya, K.; Afshar, Y.; Jeon, S. H.; Jo, S.; Brooks, B. R.; Lee, J.; Tadmor, E. B.; et al. CHARMM-GUI Nanomaterial Modeler for Modeling and Simulation of Nanomaterial Systems. *J. Chem. Theory Comput.* 2022, *18* (1), 479−493.
(132) Lee, J.; Cheng, X.; Swails, J. M.; Yeom, M. S.; Eastman, P. K.; Lemkul, J. A.; Wei, S.; Buckner, J.; Jeong, J. C.; Qi, Y.; et al. CHARMM-GUI Input Generator for NAMD, GROMACS, AMBER, OpenMM, and CHARMM/OpenMM Simulations Using the CHARMM36 Additive Force Field. *J. Chem. Theory Comput.* 2016, *12* (1), 405−413.
(133) Wu, E. L.; Cheng, X.; Jo, S.; Rui, H.; Song, K. C.; Dávila-Contreras, E. M.; Qi, Y.; Lee, J.; Monje-Galvan, V.; Venable, R. M.; et al. CHARMM-GUI Membrane Builder toward realistic biological membrane simulations. *J. Comput. Chem.* 2014, *35* (27), 1997−2004.
(134) Van Der Spoel, D.; Lindahl, E.; Hess, B.; Groenhof, G.; Mark, A. E.; Berendsen, H. J. GROMACS: fast, flexible, and free. *J. Comput. Chem.* 2005, *26* (16), 1701−1718.
(135) Kawanishi, N.; Christenson, H. K.; Ninham, B. W. Measurement of the interaction between adsorbed polyelectrolytes: gelatin on mica surfaces. *J. Phys. Chem.* 1990, *94* (11), 4611−4617.
(136) Gong, X.; Kozbial, A.; Li, L. What causes extended layering of ionic liquids on the mica surface? *Chemical Science* 2015, *6* (6), 3478−3482.
(137) Heinz, H.; Lin, T.-J.; Kishore Mishra, R.; Emami, F. S. Thermodynamically consistent force fields for the assembly of inorganic, organic, and biological nanostructures: the INTERFACE force field. *Langmuir* 2013, *29* (6), 1754−1765.
(138) Heinz, H.; Vaia, R. A.; Farmer, B. L.; Naik, R. R. Accurate Simulation of Surfaces and Interfaces of Face-Centered Cubic Metals Using 12−6 and 9−6 Lennard-Jones Potentials. *J. Phys. Chem. C* 2008, *112* (44), 17281−17290.
(139) Klauda, J. B.; Venable, R. M.; Freites, J. A.; O'Connor, J. W.; Tobias, D. J.; Mondragon-Ramirez, C.; Vorobyov, I.; MacKerell, A. D.; Pastor, R. W. Update of the CHARMM All-Atom Additive Force Field for Lipids: Validation on Six Lipid Types. *J. Phys. Chem. B* 2010, *114* (23), 7830−7843.
(140) Kadaoluwa Pathirannahalage, S. P.; Meftahi, N.; Elbourne, A.; Weiss, A. C. G.; McConville, C. F.; Padua, A.; Winkler, D. A.; Costa Gomes, M.; Greaves, T. L.; Le, T. C.; et al. Systematic Comparison of the Structural and Dynamic Properties of Commonly Used Water Models for Molecular Dynamics Simulations. *J. Chem. Inf. Model.* 2021, *61* (9), 4521−4536.
(141) Vanommeslaeghe, K.; Hatcher, E.; Acharya, C.; Kundu, S.; Zhong, S.; Shim, J.; Darian, E.; Guvench, O.; Lopes, P.; Vorobyov, I.; et al. CHARMM general force field: A force field for drug-like molecules compatible with the CHARMM all-atom additive biological force fields. *J. Comput. Chem.* 2010, *31* (4), 671−690.
(142) Vanommeslaeghe, K.; MacKerell, A. D. Automation of the CHARMM General Force Field (CGenFF) I: Bond Perception and Atom Typing. *J. Chem. Inf. Model.* 2012, *52* (12), 3144−3154.
(143) Vanommeslaeghe, K.; Raman, E. P.; MacKerell, A. D. Automation of the CHARMM General Force Field (CGenFF) II: Assignment of Bonded Parameters and Partial Atomic Charges. *J. Chem. Inf. Model.* 2012, *52* (12), 3155−3168.
(144) Guixa-González, R.; Rodriguez-Espigares, I.; Ramírez-Anguita, J. M.; Carrió-Gaspar, P.; Martinez-Seara, H.; Giorgino, T.; Selent, J. MEMBPLUGIN: studying membrane complexity in VMD. *Bioinformatics* 2014, *30* (10), 1478−1480.
(145) Humphrey, W.; Dalke, A.; Schulten, K. VMD: Visual molecular dynamics. *J. Mol. Graphics* 1996, *14* (1), 33−38.
(146) Buchoux, S. FATSLiM: a fast and robust software to analyze MD simulations of membranes. *Bioinformatics* 2017, *33* (1), 133−134.